# Atmospheric bias teleconnections in boreal winter associated with systematic SST errors in the tropical Indian Ocean

Yuan-Bing Zhao[1], Nedjeljka Žagar[1], Frank Lunkeit[1], and Richard Blender[1]

[1]Meteorologisches Institut, Universität Hamburg, Hamburg, Germany

**Correspondence:** Yuan-Bing Zhao (yuan-bing.zhao@uni-hamburg.de)

**Abstract.** Coupled climate models suffer from significant sea surface temperature (SST) biases in the tropical Indian Ocean (TIO), leading to errors in global climate predictions. In this study, we investigate atmospheric bias teleconnections caused by the TIO SST bias and their impacts on model variability. A set of century long simulations forced by idealized SST perturbations, which resemble various (monopolar or dipolar, positive or negative) persistent TIO SST biases in coupled climate models, are conducted with an intermediate complexity atmospheric model. Bias teleconnections with a focus on boreal wintertime are researched using the normal-mode function decomposition which can differentiate between balanced and unbalanced flow regimes across spatial scales. The results show that the atmospheric circulation biases caused by the TIO SST bias have the Gill-Matsuno-type pattern in the tropics and Rossby wave-train distribution in the extratropics, like the steady state response to tropical heating perturbations. The teleconnections between tropical and extratropical biases are set up by Rossby wave activity flux emanating from the subtropics. Over 90% of the bias variance is contained in zonal wavenumbers $k \leq 5$. Comparisons among experiments show that the northward shift of the SST bias away from the equator weakens the atmospheric response, but does not change its structure. Besides, the positive SST bias produces stronger bias teleconnections than the negative one of the same size and magnitude.

The response of the spatial variance (i.e., energy) to the TIO SST biases depends on dynamical regimes and spatial scales. Across all experiments, the unbalanced zonal-mean flow energy decreases, whereas its balanced counterpart increases. These changes primarily arise from the strong covariance between the circulation bias and the reference state (i.e., bias covariance). For the wave flow energy, the unbalanced and the tropical balanced parts show a synchronized response. Both increase in experiments with monopolar SST bias and decrease in that with dipolar SST bias. The increase is mainly due to the bias variance, whereas the decrease is due to a strong negative bias covariance at zonal wavenumbers $k = 1$ and 2. In contrast, the extratropical balanced wave flow energy decreases in experiments with positive SST bias (including the dipolar case) and increases in that with the negative SST bias, which is mainly due to the bias covariance at zonal wavenumber $k = 1$. The response of the interannual variance (IAV) is contingent upon the sign of the SST bias. A positive SST bias reduces the IAV, whereas a negative one increases it, regardless of dynamical regimes. Geographically, strong IAV responses are observed in the tropical Indo-west Pacific region, Australia, South and Northeast Asia, the Pacific-North America region and Europe, where the background IAVs are strong.

# 1 Introduction

The tropical Indian Ocean (TIO) plays an important role in climate variability (e.g. Schott et al., 2009; Beal et al., 2020; Hermes et al., 2019). A realistic representation of the TIO sea surface temperature (SST) in the ocean-atmosphere coupled general circulation models (CGCMs) is crucial for the accurate prediction of both local and remote climate. However, state-of-the-art CGCMs exhibit large systematic errors (biases) in the TIO SST (Li and Xie, 2012), which inevitably affect the accuracy of the atmospheric simulations (Joseph et al., 2012; Levine and Turner, 2012; Prodhomme et al., 2014). This study aims at understanding the local and, more importantly, the remote effects of the TIO SST biases, which are termed "bias teleconnections".

The TIO SST biases vary widely in amplitude and sign among the models involved in the Coupled Model Intercomparison Project (CMIP). About half of the CMIP5 models show positive SST biases over the western TIO during boreal summer (Fathrio et al., 2017; Lyon, 2020). For instance, the SINTEX-F2 model has a warm SST bias in the tropics, especially over the western TIO region (Joseph et al., 2012), and this bias is nearly constant throughout the annual cycle (Prodhomme et al., 2014). Other half of the CMIP5 models show negative SST biases over the entire TIO region throughout the year (Wang et al., 2014; Fathrio et al., 2017). For instance, the HadCM3 model has a large-magnitude, cold SST bias in winter and spring in the Arabian Sea (Turner et al., 2005; Levine and Turner, 2012). Similar cold bias is present in most CMIP6 models (Wang et al., 2022). In addition, a significant warm TIO SST bias was recently reported in the CMIP6 models, which was not evident in the CMIP5 models (Zhang et al., 2023). Furthermore, the SST biases are also coupled with the representation of the Indian Ocean Dipole (IOD) which remains overly strong in all generations of CMIP models (Cai and Cowan, 2013; Weller and Cai, 2013). The IOD-like SST biases in the majority of the CMIP5 models (Li et al., 2015) are seen even stronger in the CMIP6 models (McKenna et al., 2020).

The long-standing TIO SST biases impact the skill of climate prediction. Locally, the TIO SST biases modify the meridional SST gradient and affect the Indian summer monsoon, leading to biases in precipitation (Joseph et al., 2012; Levine and Turner, 2012; Bollasina and Ming, 2013; Annamalai et al., 2017; Prodhomme et al., 2014). Moreover, an SST increase from $26.5°C$ to $28.0°C$ has been shown by both observations and simulations to drastically change the convective response from shallow to deep convection (e.g., Gadgil et al., 1984; Roxy et al., 2014). On the other hand, SST biases also have remote impacts. Wang et al. (2014) found in CMIP5 models that local SST biases can be linked with those in far away regions. Recently, Stan et al. (2023) and Bai et al. (2023) showed that the tropical west Pacific warm bias in the Unified Forecast System global coupled model can influence the simulated North American precipitation remotely through the wave activity flux.

However, the impacts of TIO SST biases on simulated atmospheric variability are more difficult to quantify as it requires isolating the effects of the TIO SST biases from other biases and the internal variability. One way to address this challenge is to perform idealized numerical experiments using the perfect-atmosphere-model framework (e.g., Žagar et al., 2020). Such experiments by Annamalai et al. (2007) showed that the diabatic heating associated with the TIO seasonally varying SST

anomalies can generate Rossby wave packets which set up the teleconnection between the TIO and the Pacific-North American (PNA) region and impact considerably the Northern Hemisphere (NH) extratropical circulation.

The present study extends existing research of the effects of systematic errors in the TIO SST on the atmospheric variability by quantifying spatial and temporal variance changes from a global perspective. We hypothesize that TIO SST biases induce biases in the simulated atmospheric circulation not only in the tropics but also in the extratropics through tropics-extratropics coupling, and that TIO SST biases affect the spatio-temporal variability across scales. Specific questions to be addressed in this paper are as follows:

- What is the spatial structure of biases in simulated circulation in the tropics and extratropics due to the TIO SST biases? Which zonal scales are most affected?

- What are the dynamical mechanisms that connect the TIO SST bias to biases in simulated circulation?

- How do global spatial and temporal variability change in response to the TIO SST biases?

We adopt the perfect-atmosphere-model framework with an intermediate complexity climate model (Planet Simulator; Fraedrich et al., 2005), which allows us to easily interpret the model results. A reference (or control) simulation forced by observed SST is conducted and compared to sensitivity simulations forced by the same SST but augmented with SST biases in the TIO region. The scale and regime decomposition of the circulation is performed using the normal-mode function decomposition (Žagar et al., 2015). The method for studying the effects of biases on simulated variability in climate models was developed by Žagar et al. (2020). They showed that SST errors lead to large biases in circulation and interannual variability even though the atmospheric part of their CGCM is perfect. However, they studied only the total atmospheric response to globally distributed SST errors, without regime decomposition. Application of the method to CMIP6 models by Castanheira and Marques (2022) showed that the presence of the cold SST bias in North Pacific may compensate for the biases in the North Pacific barotropic atmospheric variability through influence on the excitation of the most unstable barotropic mode of the atmospheric circulation.

The rest of this paper is organized as follows. In Section 2, we describe the Planet Simulator and the experiment design, followed by the description of methods for the quantification of circulation and variability biases. The results are presented in Section 3, including the total circulation biases, the regime-dependent biases, the underlying physics of remote bias coupling and its impacts on the simulated spatio-temporal variability. The study is summarized in Section 4.

## 2  Methodology

We first present the design of numerical experiments with Planet Simulator (PLASIM; Fraedrich et al., 2005; Fraedrich and Lunkeit, 2008). This is followed by the description of the normal-mode function (NMF) decomposition and definition of quantities analysed in modal and physical space.

## 2.1 Climate model and experiment design

### 2.1.1 The model

PLASIM models the atmospheric dynamics using primitive equations in $\sigma$-coordinate, $\sigma = p/p_s$, where $p$ and $p_s$ denote the pressure and the surface pressure, respectively. The prognostic variables are vorticity, divergence, temperature, specific humidity and the logarithm of the surface pressure. The hydrostatic primitive equations are solved using the spectral transformation methods (Eliassen et al., 1970; Orszag, 1970). Unresolved processes are parameterized, which include the long-wave (Sasamori, 1968) and short-wave (Lacis and Hansen, 1974) radiation, interactive clouds (Stephens, 1978, 1984; Slingo and Slingo, 1991), moist (Kuo, 1965, 1974) and dry convection, large-scale precipitation, the horizontal and vertical diffusion (Louis, 1979; Louis et al., 1982; Laursen and Eliasen, 1989; Roeckner et al., 1992), and boundary-layer parameterization including latent and sensible heat fluxes (Louis, 1979). For more information on the model, the reader is referred to Fraedrich et al. (2005).

In this study, we run PLASIM with prescribed SST and sea ice content. We adopt a T31 horizontal resolution (approximately $3.75° \times 3.75°$ on the corresponding $96 \times 48$ Gaussian grid) and ten $\sigma$ levels: 0.038, 0.119, 0.211, 0.317, 0.437, 0.567, 0.699, 0.823, 0.924, 0.983.

The atmosphere-ocean coupling plays a crucial role in the simulation. With the SST fixed, the atmosphere and ocean surface communicate by exchanging the heat and moisture. The bulk aerodynamic formulas for the surface fluxes are

$$F_T = \rho c_p C_H |\mathbf{V}|(\mathrm{SST} - T_{\mathrm{air}}),  \tag{1}$$

$$F_q = \rho C_H C_W |\mathbf{V}|(q_{\mathrm{sea}} - q_{\mathrm{air}}),  \tag{2}$$

where $F_T$ and $F_q$ are the sensible heat flux and the moisture flux, respectively. The constant parameters in the formulas are defined as follows: $\rho$ is air density, $c_p$ is the specific heat at constant pressure, $C_H$ is the transfer coefficient for heat, and $C_W$ is the wetness factor accounting for different evaporation efficiencies due to surface characteristics. The fluxes depend on the horizontal wind speed $|\mathbf{V}|$, air temperature $T_{\mathrm{air}}$ and specific humidity $q_{\mathrm{air}}$ at the lowermost model level, and the specific humidity at sea surface $q_{\mathrm{sea}}$ which is assumed to be saturated and has a temperature equal to the SST. Given the SST, the saturation water vapor pressure $e_{\mathrm{sat}}$ is computed using the Clausius-Clapeyron equation for SST in degrees Celsius as

$$e_{\mathrm{sat}} = 610.78 \exp\left(\frac{17.27\mathrm{SST}}{\mathrm{SST} + 237.30}\right). \tag{3}$$

Then $q_{\mathrm{sea}}$ is produced making use of instantaneous value of surface pressure $p_s$ as

$$q_{\mathrm{sea}} = \frac{\epsilon e_{\mathrm{sat}}}{p_s - (1 - \epsilon)e_{\mathrm{sat}}}, \tag{4}$$

where $\epsilon$ is the ratio of the gas constant for dry air $R_{\mathrm{d}}$ and water vapor $R_{\mathrm{v}}$ ($\epsilon = R_d/R_v$). A positive $F_T$ means heat is flowing from the surface to the atmosphere. A positive $F_q$ means water is evaporating from the surface with latent heat. Both terms exhibit seasonal variations. The globally averaged climatological annual mean $F_T$ in PLASIM forced with SST from the ERA-20C reanalyses (Poli et al., 2016) is estimated to be 20.5 W m$^{-2}$ and the seasonal variation of $F_T$ spans from -14.2% to 15.4%

120   of the annual mean. The globally averaged climatological annual mean $F_q$ is measured at 2.8 kg m$^{-2}$ day$^{-1}$, corresponding to
a latent heat flux of 81.2 W m$^{-2}$, and the seasonal variation of $F_q$ ranges from -4.4% to 6.6% of the annual mean.

The fluxes at the sea surface are closely coupled with the cumulus convection. In PLASIM, convection is parameterized by
a Kuo-type scheme (Kuo, 1974), where an important quantity involved is the net precipitation rate which is proportional to the
net amount of the horizontal moisture flux convergence (MFC) plus the moisture supply by surface evaporation (i.e., $F_q$)

$$125 \quad P_r = -\frac{p_s}{g} \int_0^1 \nabla \cdot (q\mathbf{V}) \mathrm{d}\sigma + F_q . \tag{5}$$

The above equations show that a systematic local increase in SST will lead to locally more upward sensible heat and moisture
flux, which will lower the near-surface moist static stability. Stronger convection and more precipitation ($P_r$) will occur, leading
to greater latent heat release and stronger effects on atmospheric circulation.
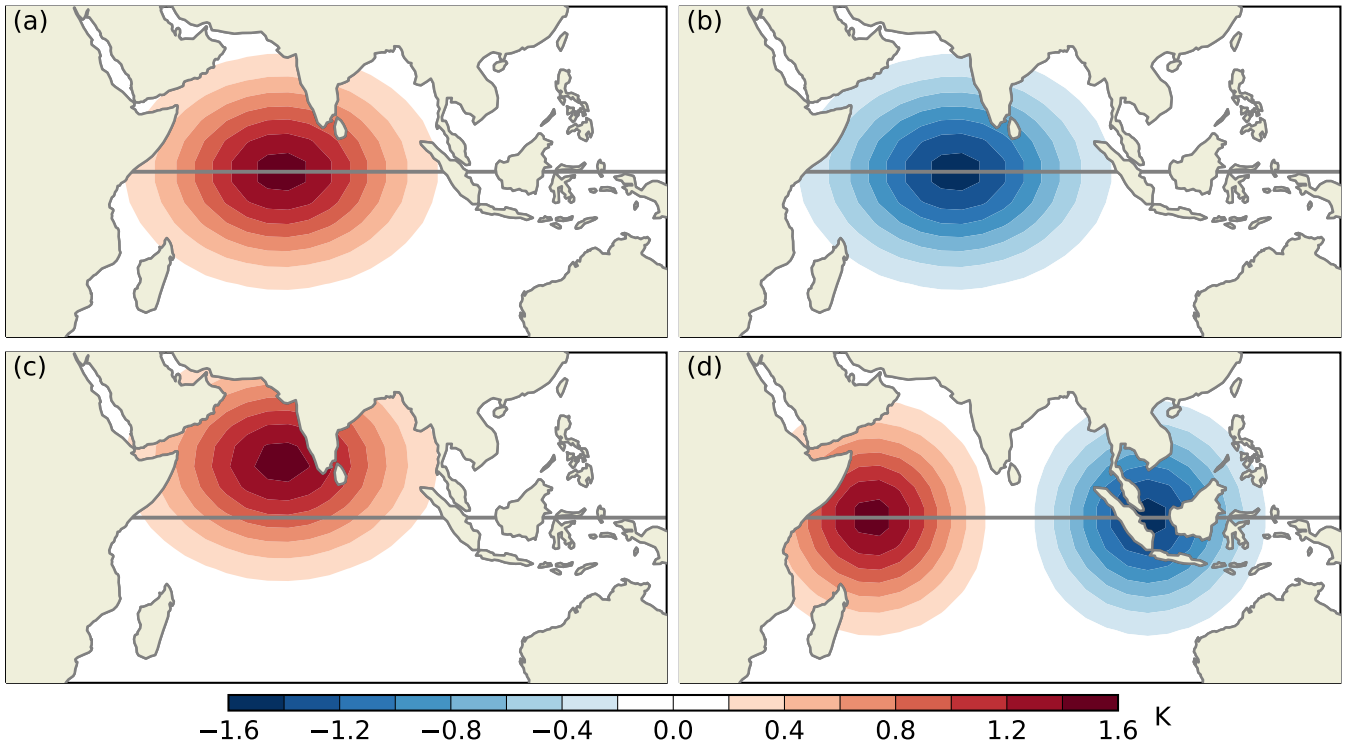
**Figure 1.** SST biases (in K) used in the sensitivity experiments: (a) EXP_POS, (b) EXP_NEG, EXP_10N, and EXP_IOD. The gray line
marks the equator.

### 2.1.2 Experiment design

130 A set of century long simulations are carried out using a perfect-model framework. In this framework, the only difference between the reference and sensitivity simulations is the SST perturbation in the Indian Ocean which represents the climate model SST bias. Differences between the simulations therefore originate from differences in the TIO SST.

The reference simulation is forced with the time-varying monthly mean SST including interannual variations from the ERA-20C reanalyses (Poli et al., 2016). Four sensitivity experiments apply the same SST with addition of time-constant perturbations 135 in the TIO region that mimic TIO SST biases found in the CGCMs (e.g., Li et al., 2015; Fathrio et al., 2017; Lyon, 2020). In other words, the steady SST perturbations in this study represent the SST biases (or systematic errors).

**Table 1.** Configurations of the SST biases.

| Experiments | $T_0$ (in K) | $\lambda_0$ | $\varphi_0$ | $\sigma_x$ | $\sigma_y$ |
|---|---|---|---|---|---|
| EXP_POS | 1.5 | 70° E | 0° | 20 | 15 |
| EXP_NEG | -1.5 | 70° E | 0° | 20 | 15 |
| EXP_10N | 1.5 | 70° E | 10° N | 20 | 15 |
| EXP_IOD | 1.5/-1.5 | 55° E/105° E | 0° | 15 | 15 |

The spatial structure of the SST perturbation is given by

$$\Delta \text{SST}(\lambda, \varphi) = \begin{cases} T_0 \exp\left[-\frac{(\lambda-\lambda_0)^2}{\sigma_x{}^2} - \frac{(\varphi-\varphi_0)^2}{\sigma_y{}^2}\right], & |\Delta \text{SST}| > 0.05; \\ 0, & \text{otherwise;} \end{cases} \tag{6}$$

where $T_0$ determines the maximal magnitude, $(\lambda_0, \phi_0)$ specifies the longitude and latitude of the center location respectively, 140 and $\sigma_x$ and $\sigma_y$ define the perturbation extent. The parameters of the four perturbations are listed in Table 1.

The distributions of SST perturbations are shown in Fig. 1. In one experiment, a monopolar SST perturbation with a maximum of +1.5 K is centered at the equator and covers the entire TIO region (Fig. 1a). Another one applies the same SST perturbation but with the opposite sign (i.e., monopolar negative SST bias; Fig. 1b). For convenience, we refer to this experiment as EXP_NEG and the previous one as EXP_POS. The third experiment is the same as EXP_POS but the SST perturbation 145 is shifted 10° northward, and the experiment is labeled as EXP_10N (Fig. 1c). The forth simulation applies a dipolar SST perturbation which mimics the IOD-type bias (e.g., Cai and Cowan, 2013; McKenna et al., 2020) and is referred to as EXP_IOD (Fig. 1d). In the equatorial Indian Ocean, the SST peaks in April at about 29.5 °C and minimizes in December, around 28 °C. In other words, the seasonal variation is about 1.5 °C, equal to the amplitude of the SST perturbation used in this study.

These SST perturbations are similar to, but not the same as, the SST biases in the coupled climate models in terms of the 150 center location, spatial extent and magnitude. The ones used in EXP_POS and EXP_IOD have their counterparts in CMIP5 models (see Fig. 4 in Lyon (2020)). Those in EXP_NEG and EXP_10N are primarily used to study the sensitivity of the response to the sign and meridional location of the SST bias, respectively.

For each experiment, the model starts on 1 January 1901 and the simulation ends on 31 December 2010. The initial condition comes from a 40-year spin-up run (i.e., an equilibrium state) forced by the climatological monthly mean ERA-20C SST (without interannual variation). In the reference simulation, the heat fluxes at the Earth's surface and the top of the atmosphere are found to be balanced (i.e., zero total heat flux) throughout the integration and the total atmospheric energy (kinetic energy plus potential energy) is conserved, even during the initialization. When a strong SST bias is applied, it will lead to the breakdown in the model's surface-top heat flux balance during the first several months of the integration (not shown), which results in a net energy input (output) into (from) the atmosphere. After this short period, the surface-top heat flux balance recovers without further net energy input (output) into (from) the atmosphere, and the atmospheric total energy will remain at the level it attains. In this study, the SST bias applied is however too weak to affect the overall heat flux balance, and the total atmospheric energy is conserved over time. But note that the weak SST bias can result in notable modifications to the available potential energy and the kinetic energy, which are the primary focus of this study.

In addition, the atmospheric circulation bias can be established in the first decade, but the atmospheric variability takes several decades to become equilibrium. We therefore discard the first 30 integration years and use the last 80 years (1931-2010) in the analysis.

## 2.2 Modal analysis

The NMF decomposition of the PLASIM simulations is performed using the MODES software (Žagar et al., 2015). The global circulation are decomposed in terms of the Hough harmonics which provide scale and regime information. Here we summarise the concept and refer the reader to Žagar et al. (2015) for details. Once the circulation is decomposed, statistics of biases and variances can be carried out in modal (or spectral) space as outlined below.

### 2.2.1 Circulation decomposition of balanced and unbalanced components

The scale and regime decomposition of the 3D global circulation relies on the representation of the global baroclinic atmosphere in terms of $M$ global shallow-water systems, each characterized by its own fluid depth for the horizontal motions that is known as the equivalent depth. The oscillations of the horizontal wind and geopotential height fields in various systems are coupled through equivalent depth, denoted as $D$, with the vertical structure equation. Given a vertical mode $m$ ($m = 1, ..., M$), the horizontal motions are represented by a series of Hough harmonics which are the product of the Hough vector functions in the meridional direction and plane waves in the zonal direction. The complex Hough expansion coefficient $\chi_n^k(m)$, which represents the two wind components $(u, v)$ and the geopotential height $h$, is obtained as

$$\chi_n^k(m) = \frac{1}{2\pi} \int_0^{2\pi} \int_{-1}^{1} \left( \mathbf{S}_m^{-1} \sum_{j=1}^{J} (u, v, h)^T G_m(j) \right) \cdot [\mathbf{H}_n^k(m)]^* \, d\mu \, d\lambda, \tag{7}$$

where the asterisk ($*$) denotes the complex conjugate. Equation (7) describes a two-step procedure which consists of the vertical projection (within the parenthesis) followed by the horizontal projection. The vertical structure functions $G_m(j)$ are orthogonal and solved using the finite difference method for the atmosphere discretized into $J$ $\sigma$-levels. The basis functions

for the horizontal projection are the Hough harmonics, denoted by $\mathbf{H}_n^k(\lambda, \varphi; m)$. For any given vertical mode, the Hough harmonics are characterized by two indices, the zonal wavenumber $k$ and the meridional mode index $n$. The scaling matrix $\mathbf{S}_m$ is a $3 \times 3$ diagonal matrix which makes the input data after the vertical projection dimensionless. Parameters $\lambda$ and $\varphi$ stand for the geographical longitude and latitude, respectively, whereas $\mu = \sin(\varphi)$.

A discrete solution of Eq. (7) is obtained by replacing the integration with a finite series of the Hough harmonics, including the zonal-mean state, $K$ zonal waves and $R$ meridional modes which combine $N_R$ balanced (BAL) or Rossby modes, $N_E$ eastward-propagating inertio-gravity (EIG) modes, and $N_W$ westward-propagating inertio-gravity (WIG) modes ($R = N_R + N_E + N_W$). Here we use a truncation similar to the PLASIM model, that is, $K = 30$, $M = 10$ and $N_R = N_E = N_W = 30$, meaning 30 meridional modes for each of the wave species. This means that our decomposition is complete and the statistics defined next accounts for the complete variance (or energy) in the system. The projection in this study is based on monthly mean data.

The decomposition (or filtering) of the circulation is an inverse process of the projection. One can filter any component of the circulation by selecting the corresponding Hough coefficients and reconstructing the component in physical space. In this way, the circulation can be decomposed into balanced and unbalanced components, with further decomposition into parts such as the Kelvin wave circulation, $n = 1$ Rossby wave circulation, and so on.

### 2.2.2 Statistics in modal space

The second moments of the circulation are evaluated in terms of Hough coefficient $\chi_\nu(t)$, where a single modal index $\nu = (k, n, m)$. The total (kinetic plus available potential) energy, or the spatial variance, contained in mode $\nu$ per unit area at time step $t$ can be defined as (Žagar et al., 2020)

$$I_\nu(t) = \frac{1}{2} g D_m |\chi_\nu(t)|^2, \tag{8}$$

with $D_m$ the equivalent depth of vertical mode $m$. The energy of the time-mean state (i.e., climatological energy) is

$$E_\nu = I(\overline{\chi_\nu}) = \frac{1}{2} g D_m |\overline{\chi_\nu}|^2, \qquad \text{where} \qquad \overline{\chi_\nu} = \frac{1}{N} \sum_{t=1}^{N} \chi_\nu(t). \tag{9}$$

The temporal variance in modal space can be defined as

$$V_\nu = \frac{1}{N} \sum_{t=1}^{N} g D_m |\chi_\nu(t) - \overline{\chi_\nu}|^2. \tag{10}$$

As shown by Žagar et al. (2020), the global integration of $V_\nu$ is equivalent to the integral of the temporal variance in physical space

$$\sum_k \sum_n \sum_m V_\nu = \sum_i \sum_j w(\lambda_i, \varphi_j) \sum_{m=1}^{M} \left[ S_m^u + S_m^v + S_m^h \right]. \tag{11}$$

Here, $w(\lambda_i, \varphi_j)$ denotes the Gaussian weight, and

$$S_m^u = gD_m Var(\tilde{u}_m), \quad S_m^v = gD_m Var(\tilde{v}_m), \quad S_m^h = gD_m Var(\tilde{h}_m), \tag{12}$$

where $\tilde{u}_m$, $\tilde{v}_m$ and $\tilde{h}_m$ represent the non-dimensionalized winds and height field after the vertical projection, and $Var(x) = \frac{1}{N}\sum_{t=1}^{N}|x(t) - \overline{x}|^2$ denotes the temporal variance of any scalar variable $x$ at location $(\lambda_i, \varphi_j)$.

215     Assuming ergodicity, the difference between the time-mean energy $\overline{I_\nu}$ and the energy of the mean state $E_\nu$ is equal to half the temporal variance (Žagar et al., 2020)

$$\overline{I_\nu} - E_\nu = \frac{1}{2}V_\nu. \tag{13}$$

Defining the time-mean energy of mode $\nu$ in the sensitivity simulation as $\overline{I_\nu^S}$ and that in the reference simulation as $\overline{I_\nu^R}$, we obtain

220     $$\overline{I_\nu^S} - \overline{I_\nu^R} = \left[E_\nu^S - E_\nu^R\right] + \frac{1}{2}\left[V_\nu^S - V_\nu^R\right], \qquad \text{or} \qquad \Delta\overline{I_\nu} = \Delta E_\nu + \frac{1}{2}\Delta V_\nu. \tag{14}$$

Superscripts $S$ and $R$ in Eq. (14) denote the sensitivity and reference simulations, respectively. It states that changes in the time-mean energy are attributed to changes in the climatological state $\Delta E_\nu$ and changes in the temporal variance $\Delta V_\nu$, allowing for an assessment of the variance budget associated with the SST bias. With the circulation bias in mode $\nu$ defined as

$$\overline{\Delta\chi_\nu} = \frac{1}{N}\sum_{t=1}^{N}\left[\chi_\nu^S(t) - \chi_\nu^R(t)\right], \tag{15}$$

225     $\Delta E_\nu$ can be decomposed into two parts, $B_\nu$ and $P_\nu$, called the bias variance and covariance respectively, defined as

$$B_\nu = \frac{1}{2}gD_m\left|\overline{\Delta\chi_\nu}\right|^2 \quad \text{and} \quad P_\nu = \frac{1}{2}gD_m\left(\overline{\Delta\chi_\nu}\overline{\chi_\nu^R}^* + \overline{\Delta\chi_\nu}^*\overline{\chi_\nu^R}\right), \quad \text{with} \quad \Delta E_\nu = B_\nu + P_\nu. \tag{16}$$

The bias covariance $P_\nu$ is computed between the bias $\overline{\Delta\chi_\nu}$ and the time-averaged reference state $\overline{\chi_\nu^R}$. These two terms indicate the amplitude ($B_\nu$) and phase ($P_\nu$) of the bias. To see this, let $\overline{\chi_\nu^R} = \left|\overline{\chi_\nu^R}\right|e^{i\theta_A}$ and $\overline{\Delta\chi_\nu} = \left|\overline{\Delta\chi_\nu}\right|e^{i\theta_B}$, then the bias covariance becomes

230     $$P_\nu = gD_m\left|\overline{\chi_\nu^R}\right|\left|\overline{\Delta\chi_\nu}\right|\cos(\Delta\theta), \tag{17}$$

where $\Delta\theta = \theta_B - \theta_A$ denoting the phase difference between bias and reference state. If $|\Delta\theta| < \pi/2$, $P > 0$; otherwise, $P \leq 0$. If the model is bias free (i.e., $\overline{\Delta\chi_\nu} = 0$), both terms vanish.

## 3   Results

In this study, we aim at understanding the general principle behind the bias teleconnection rather than its seasonal variation.
235     Indeed, the circulation bias in the tropics (25°S-25°N) has similar pattern throughout the year but with varying magnitude, and the extratropical biases are primarily observed in the Northern Hemisphere during boreal winter and in the Southern Hemisphere during boreal summer. In transition seasons (spring and autumn), extratropical biases exist in both Hemispheres with similar magnitude. We narrow our focus exclusively to the boreal wintertime (December-January-February; DJF). In the following, we first validate the reference simulation before discussing the bias and variability changes in sensitivity simulations.
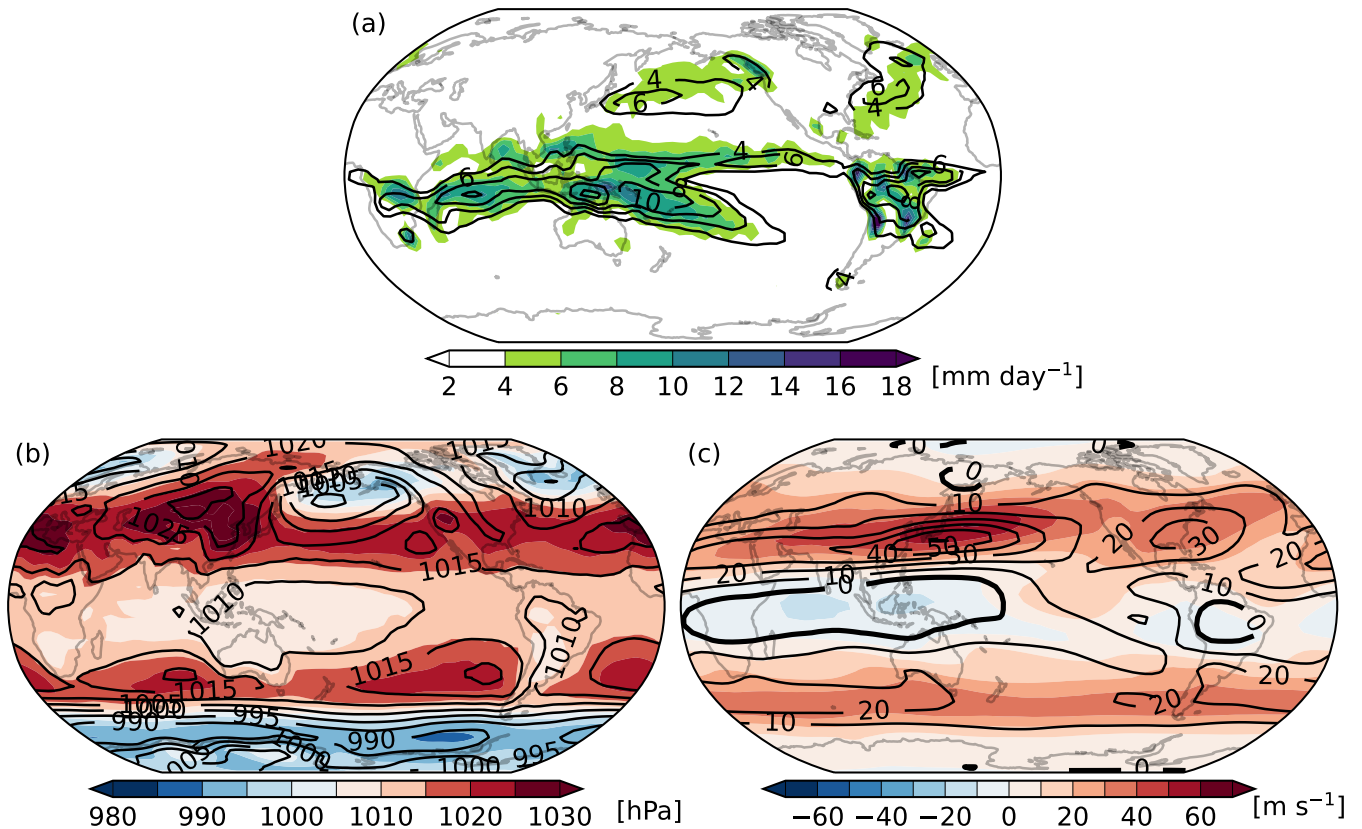
**Figure 2.** Long-term (1931-2010) mean DJF fields of the reference simulations (colors) overlaid with the ERA-20C reanalyses (contours): (a) total precipitation (in mm day$^{-1}$), (b) mean sea level pressure (in hPa) and (c) 250 hPa zonal wind (in m s$^{-1}$).

## 3.1 Model validation

Figure 2 displays the climatology DJF fields of the reference simulation and the ERA-20C reanalyses. Overall, PLASIM is able to simulate the precipitation and the general circulation with correct patterns and magnitudes. For instance, the strong precipitation centers in the tropics are well simulated, which indicate the Inter-Tropical Convergence Zone (ITCZ) and the South Pacific Convergence Zone (SPCZ) (Fig. 2a). In midlatitudes, strong precipitation is seen in the North Pacific and North Atlantic, where the atmospheric storm tracks are located. As for the circulation, the high-low pressure systems at the sea level (Fig. 2b) and zonal wind in the upper troposphere (Fig. 2c) are also well reproduced. But, there are also some discrepancies between the PLASIM simulation and the reanalyses. Particularly, the precipitation centers in the Bay of Bengal and the South China Sea are not well simulated (Fig. 2a). Besides, the precipitation in midlatitudes is generally underestimated and the precipitation center over the North Pacific shifts northward compared with the reanalysis, which should be attributed to the northward shift of the Aleutian low (Fig. 2b) and the jet stream (Fig. 2c) over the North Pacific in the simulation. Nevertheless, these discrepancies are not unexpected given that PLASIM is a model of intermediate complexity.

In what follows, we validate sensitivity simulations against the reference simulation and according to Eq. (15) call their time (1931-2010) averaged difference "bias".
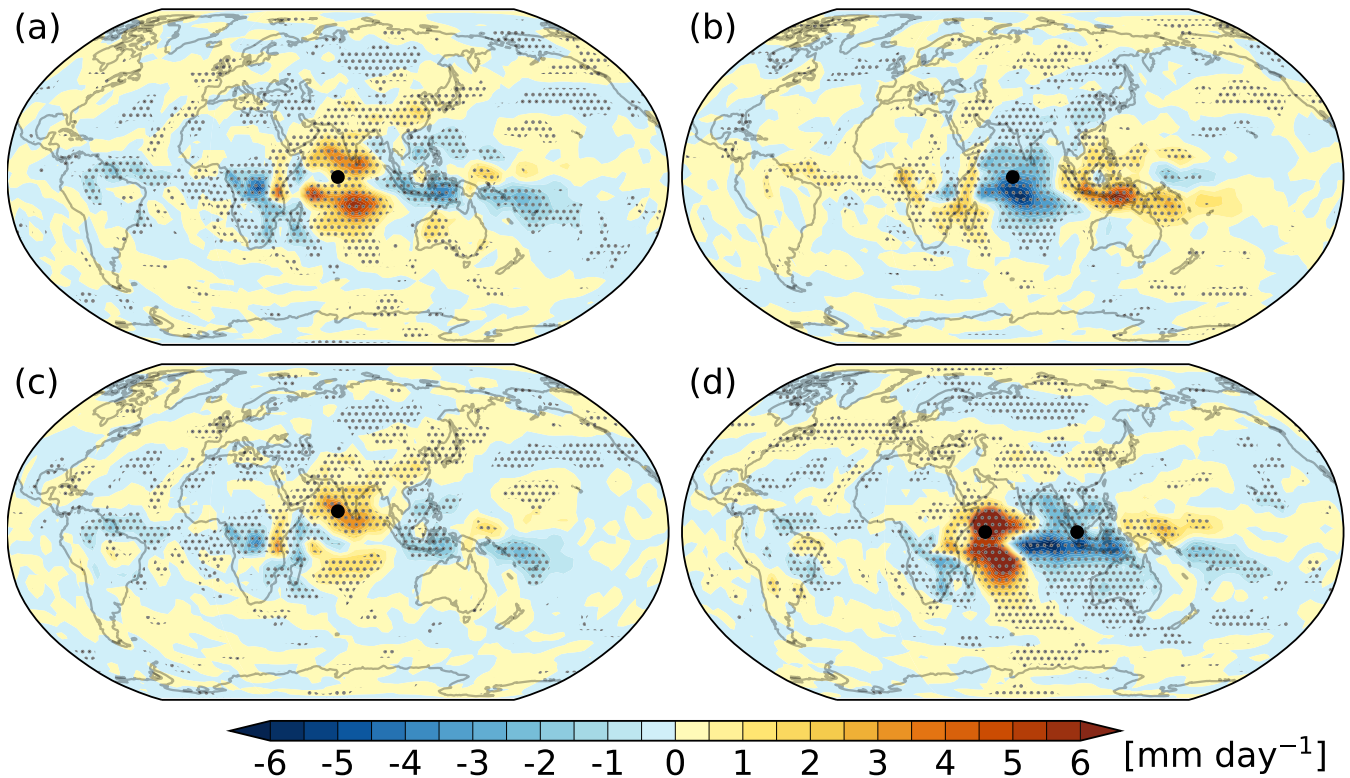
**Figure 3.** Distribution of the DJF precipitation biases (in mm day$^{-1}$): (a) EXP_POS, (b) EXP_NEG, (c) EXP_10N and (d) EXP_IOD. Dotted area shows the region of biases statistically significant at 0.05 level using the Student's $t$-test. The large black dot in each panel marks the location of the SST bias center (the same below).

## 3.2 Precipitation biases

255    Figure 3 shows the distribution of the DJF total precipitation biases. The strongest biases are confined in the tropics. One prominent common feature among the four experiments is the wet (dry) bias in the area where positive (negative) SST biases are applied. As explained in Section 2.1.1, this is attributed to the response of the local air-sea interaction to the SST bias. The warm SST bias results in locally more upward sensible and moisture fluxes at the surface, lowering the near-surface static stability, enhancing the low-level moisture convergence (Lindzen and Nigam, 1987; Back and Bretherton, 2009), and therefore

260    bringing more deep convection and precipitation. The cold SST bias leads to opposite results, namely dry bias in the TIO region (Fig. 3b). The northward shift of the SST bias does not have much impact on the spatial structure of the precipitation biases, but reduces the magnitude (Fig. 3c). As for the dipolar SST bias, it causes much stronger precipitation biases in the TIO region (Fig. 3d) than monopolar SST biases (Figs. 3a-3c).
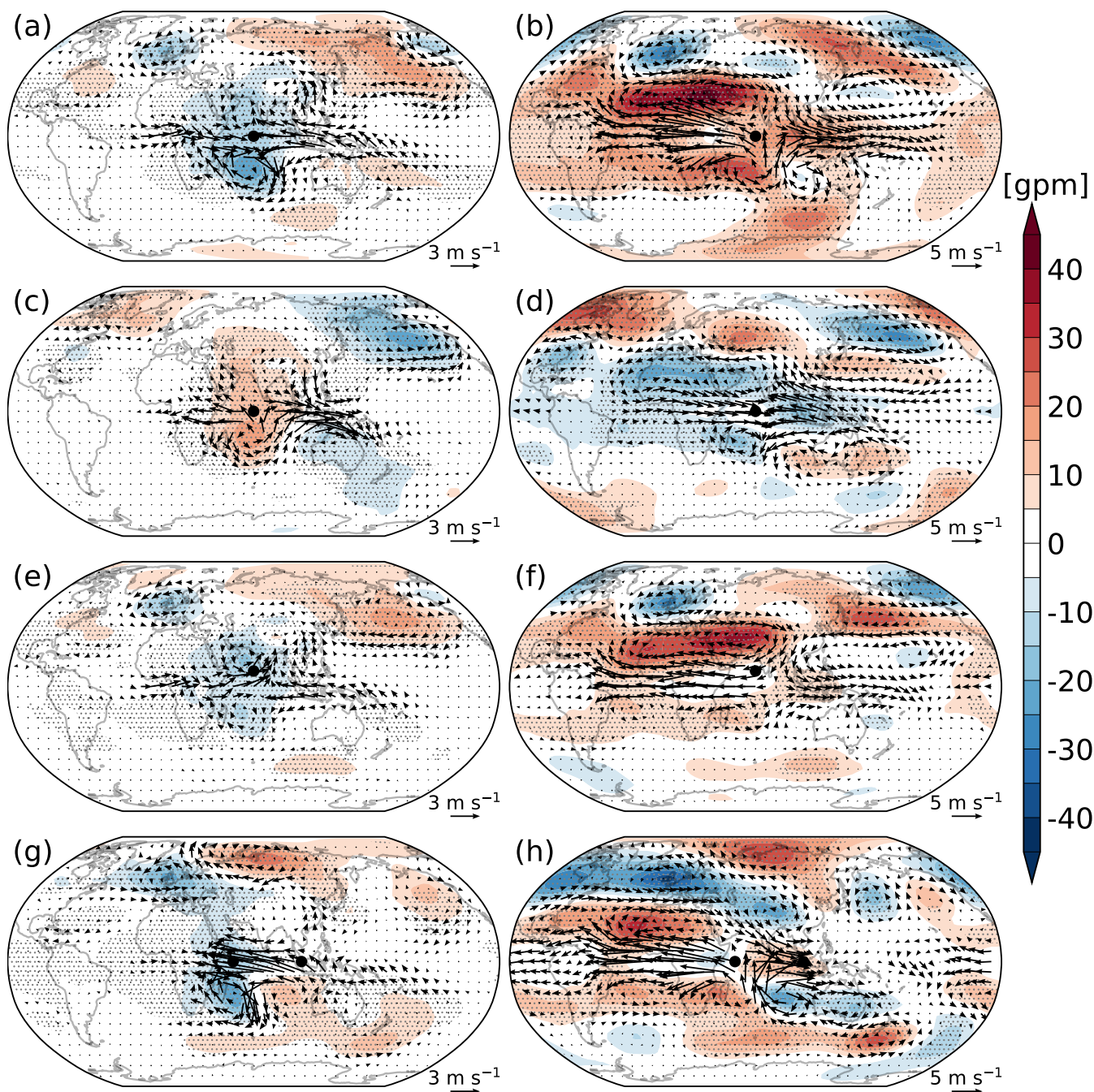
**Figure 4.** Total circulation biases in (a,b) EXP_POS, (c,d) EXP_NEG, (e,f) EXP_10N and (g,h) EXP_IOD at (left) $\sigma = 0.924$ and (right) $\sigma = 0.211$. Vectors stand for winds (in m s$^{-1}$) and colors for geopotential height (in gpm). Dotted area shows the region of geopotential height biases statistically significant at 0.05 level using the Student's $t$-test.

Apart from the local response, significant biases are also seen in remote areas. Looking at EXP_POS (Fig. 3a), strong dry biases are found roughly along the equator to the west and east of the TIO region. In particular, rain band associated with the SPCZ is significantly reduced. Significant precipitation biases are also visible in the extratropics (e.g., East and North Asia and North Pacific), but their magnitudes are small. These nonlocal precipitation biases are associated with the circulation biases caused by the SST biases. We will come back to this later.

## 3.3 Circulation biases

In this section, we discuss biases in circulation decomposed in balanced (Rossby, including the mixed Rossby-gravity (MRG) modes) and unbalanced (IG, including the Kelvin modes) components. But first we present the total circulation bias, that is, the sum of the balanced and unbalanced components.

### 3.3.1 Total biases

Biases in the DJF horizontal circulation are shown in Fig. 4. In all sensitivity experiments, strong biases are mainly observed in the tropics and the Northern Hemisphere. In the experiment with positive (negative) SST biases, anomalous winds associated with negative (positive) geopotential height biases converge (diverge) at lower levels in the TIO area, whereas at upper levels the winds diverge (converge); this indicates the Walker circulation bias on the zonal section which is closely associated with the strong precipitation biases in the tropics (Fig. 3). In the extratropics, the bias centers at lower and upper levels are generally in phase, indicating barotropic structure. These centers are organized as stationary Rossby wave-trains linking the subtropics and mid-to-high latitudes, which bear some resemblance to the simulation by Annamalai et al. (2007). They should account for the extratropical precipitation biases (Fig. 3). For instance, in EXP_POS, one can see a cyclonic circulation bias and an anticyclonic circulation bias over the North Pacific (Fig. 4b), accompanied by positive and negative precipitation biases, respectively (Fig. 3a). In comparison, EXP_POS (Figs. 4a and 4b) and EXP_NEG (Figs. 4c and 4d) have similar bias distributions but opposite signs. Despite the northward shift of SST bias in EXP_10N, its circulation biases (Figs. 4e and 4f) resemble those in EXP_POS (Figs. 4a and 4b), albeit with smaller amplitude. Previous studies have shown that SST changes in tropical ascending regions are more efficient at generating global impacts (e.g., Zhou et al., 2017). In DJF, the ascending branch of the Hadley circulation is located slightly south of the equator. Thus, as SST bias moves northward away from the equator, it becomes less efficient at impacting the atmosphere. The strongest extratropical bias centers are mainly observed over the Pacific-North America (PNA) region in all experiments except EXP_IOD where they are seen over North America, North Atlantic, Europe and Northeast Asia (Figs. 4g and 4h).

It is difficult to tell the changes in the zonal-mean flow from Fig. 4. In fact, the unbalanced zonal-mean flow is dominated by the Hadley circulation (Pikovnik et al., 2022). It weakens with positive SST bias (EXP_POS, EXP_10N, and EXP_IOD) whereas strengthens with monopolar negative SST bias (EXP_NEG). But in any case, the overall change is weak compared to the reference state. Regarding the balanced part, the diabatic heating induced by the positive SST bias warms the atmosphere and raises the geopotential field, particularly in the subtropics. This is accompanied by the a strengthening of the westerlies in the midlatitudes and the easterlies in the tropics. The maximum change in the upper troposphere can reach 1.5 m s$^{-1}$. The

opposite occurs in monopolar negative SST bias forcing. The changes in the zonal-mean fields are further elaborated in the Supplement.

In short, SST biases in the TIO region cause anomalous deep convection accompanied by anomalous diabatic heating, which ultimately leads to circulation biases worldwide. Nevertheless, the circulation biases are yet to be fully understood since the balanced and unbalanced components are mixed together, especially in the tropics. In the following, we decompose the total biases into the balanced and unbalanced regimes using the MODES software for further discussions.

### 3.3.2 Regime decomposition of the biases
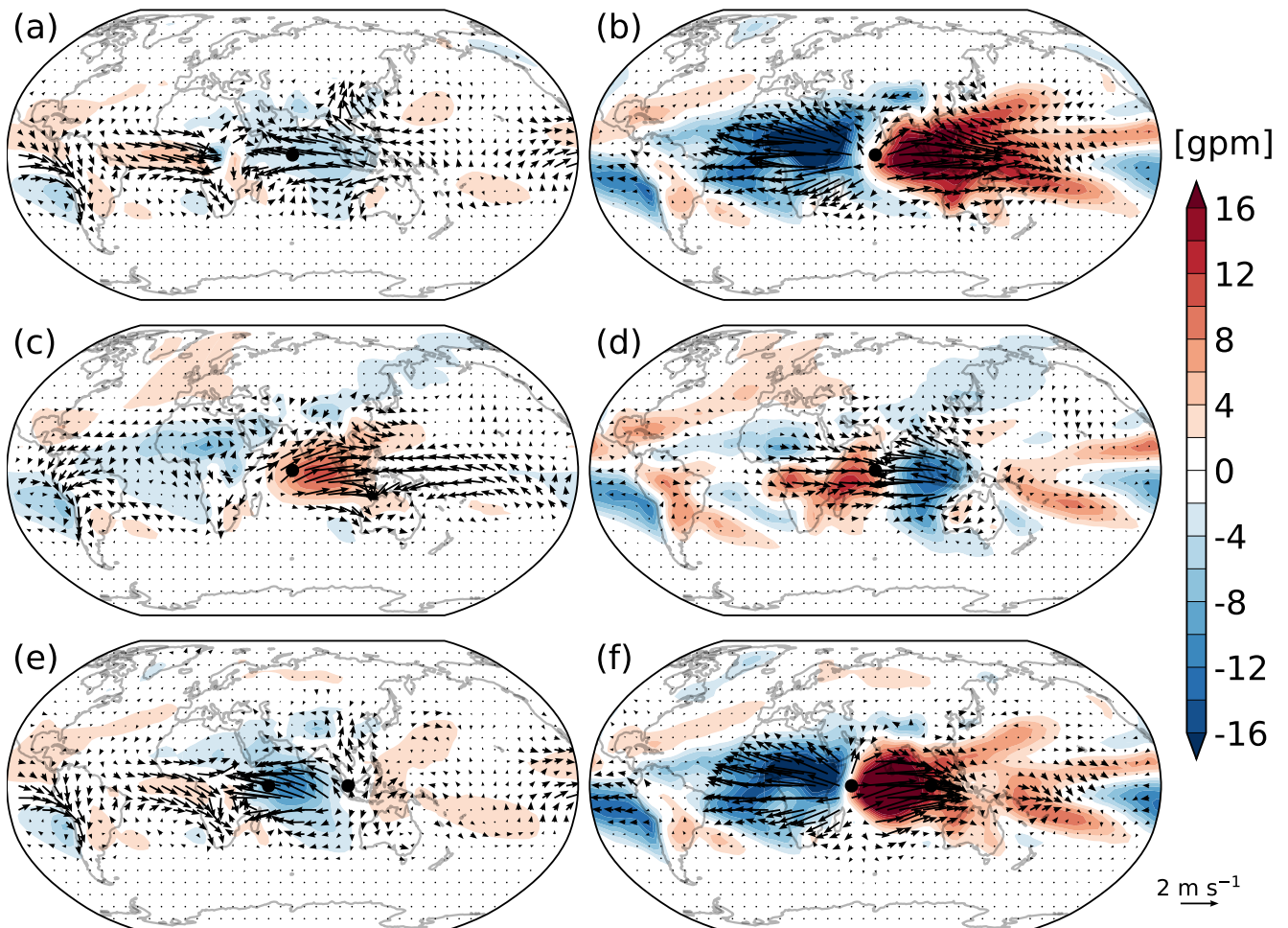
**Figure 5.** The unbalanced wave biases in (a,b) EXP_POS, (c,d) EXP_NEG and (e,f) EXP_IOD at (left) $\sigma = 0.924$ and (right) $\sigma = 0.211$. Vectors stand for winds (in m s$^{-1}$) and colors for geopotential height (in gpm). The zonal-mean ($k = 0$) mode has been excluded.
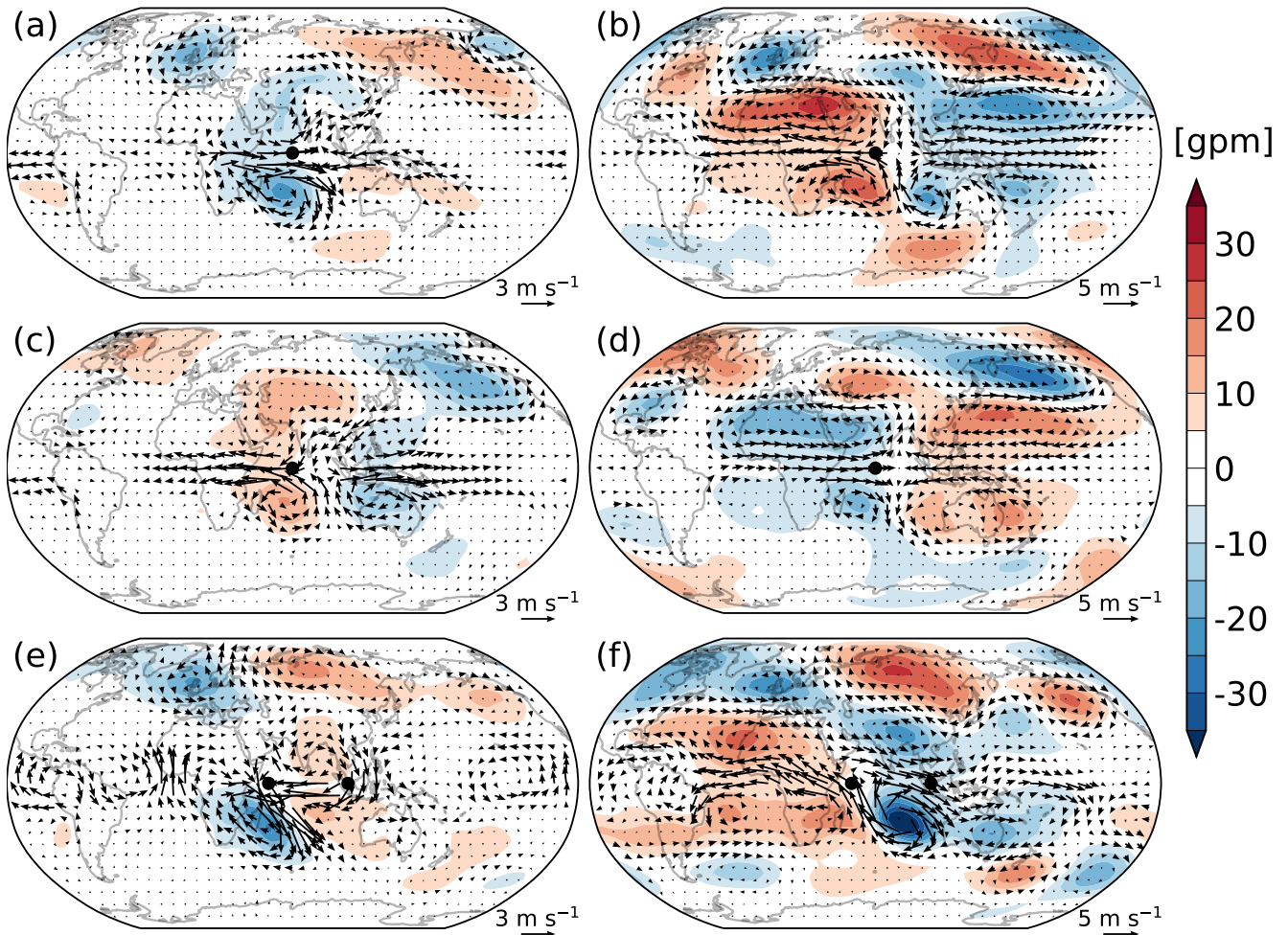
**Figure 6.** Same as Fig. 5, but for the balanced wave biases.

We first look at the unbalanced biases which are displayed in Fig. 5. They are reconstructed with the Hough coefficients
305 of all unbalanced modes except the zonal-mean ($k = 0$) mode since we are more interested in the wave part. The EXP_10N
is not shown since it has quite similar results to EXP_POS (see Fig. 4). One common feature among these experiments is
that the unbalanced biases are mainly confined in lower latitudes. They have the characteristics of the baroclinic Kelvin waves
(Matsuno, 1966). The geopotential height field exhibits a dipolar structure along the equator where the wind and mass fields are
generally balanced in the meridional direction and unbalanced in the zonal direction. This feature is however not clearly seen
310 in the total fields (Fig. 4). In EXP_POS, the winds converge towards the warm area along the equator at the lower level (Fig.
5a), whereas at the upper level the winds flow zonally away from the area (Fig. 5b). EXP_NEG has similar bias distributions
to EXP_POS, but with opposite signs and smaller magnitudes (Figs. 5c and 5d), implying the non-linearity of the response to

positive and negative SST biases (e.g., Lunkeit and von Detten, 1997). In EXP_IOD (Figs. 5e and 5f), the Kelvin-type biases shift a bit westward compared with EXP_POS.

315    Figure 6 shows the balanced biases. They also share a number of common features among the four experiments. The bias fields are characterized by a quadrupole in the tropics and subtropics (referred to from now on as TROP). In the extratropics (referred to from now on as EXTR), alternatively distributed cyclones and anticyclones organized in stationary Rossby wave-train-like pattern are observed. Vertically, the TROP biases are baroclinic, similar to their unbalanced counterparts (Fig. 5). In contrast, the EXTR biases are generally barotropic. The biases in EXP_POS (Figs. 6a and 6b) and EXP_NEG (Figs. 6c and 6d)

320    have similar distributions but opposite signs. In extratropics, strong biases are particularly seen in the PNA region. Although EXP_IOD adopts a dipolar SST bias, its TROP bias fields are largely defined by the positive SST bias (Figs. 6e and 6f). The bias centers in EXP_IOD as a whole shift westward compared to the other experiments. This is consistent with previous studies that the atmospheric response to a dipolar heating in the tropics is mostly defined by the positive pole (Kosovelj et al., 2019). In contrast to the other experiments, the EXTR biases in EXP_IOD are strong over North America and Eurasia but relatively

325    weak over North Pacific (Fig. 6f).

### 3.3.3    Mechanism of bias teleconnections

The TROP and EXTR balanced biases exhibit teleconnections, which can be demonstrated by using the the stationary wave activity flux (WAF; Plumb, 1985) and the Rossby wave source (RWS; Sardeshmukh and Hoskins, 1988). The WAF is an indicator of the propagation of the Rossby wave activity and the RWS denotes the wave forcing which takes the form: $-\nabla \cdot$

330    $\mathbf{v}_\chi(\zeta + f)$, with $\mathbf{v}_\chi$ representing the divergent wind, $\zeta$ the relative vorticity and $f$ the Coriolis parameter. Positive (negative) RWS indicates cyclonic (anticyclonic) wave forcing. The bias-related WAF and RWS are evaluated at 250 hPa. In the evaluation of WAF, the stationary wave fields are referred to as the balanced biases with the zonal-mean part removed. The RWS bias is computed as the time-mean difference between the sensitivity and the reference simulations.

    The maps of RWS and WAF associated with balanced wave biases are displayed in Fig. 7. The major feature is the wave

335    propagation indicated by WAF over Aisa and the PNA region. In EXP_POS, there are two wave paths. One (the northern path) originates in Asia and spreads northeastward and then eastward; the other (the southern path) originates in the subtropical North Pacific and propagates northeastward. The two wave paths merge over the northeast Pacific and then propagate eastward across the North America and North Atlantic, and finally terminate over North Africa (Fig. 7a). EXP_NEG has similar wave propagation to EXP_POS, but its northern wave path is very weak (Fig. 7b). In EXP_10N, the northern wave path is similar to

340    that of EXP_POS, but the southern wave path no longer exists (Fig. 7c). The wave-train in EXP_IOD originates in South Asia. It first spreads northeastward and then eastward across the North Pacific (Fig. 7d). The wave route in EXP_IOD is much zonal, which may be due to the wave being trapped by the jet stream (Zhang and Liang, 2022). The termination of the Rossby waves over America in EXP_IOD is probably due to the zonal inhomogeneity of the jet stream, which is very weak to the west coast of North America and does not support Rossby wave propagation.

345    In addition, one can see that the wave propagation in all experiments originates from the subtropics where RWS is strong. The strong RWSs first generate the systems in the subtropics, which then disperse northeastward. For instance, over mid-to-east
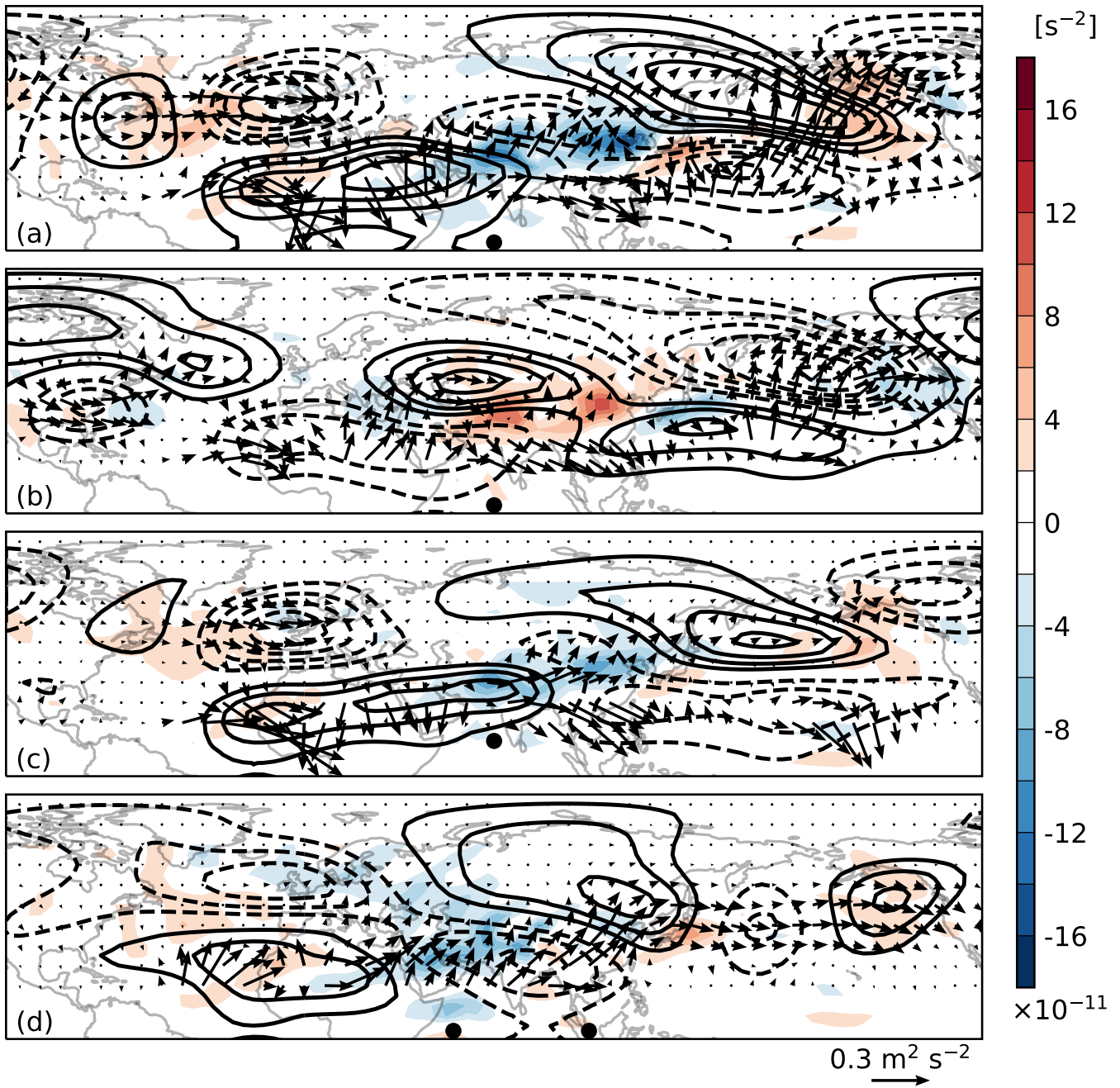
**Figure 7.** Horizontal distribution of the 250 hPa stationary wave activity flux (vectors, m² s⁻²) and Rossby wave source (colors, s⁻²) in DJF: (a) EXP_POS, (b) EXP_NEG, (c) EXP_10N, and (d) EXP_IOD. Black contours show the balanced geopotential height biases. The contour interval is 5 gpm. Negative values are indicated with dashed lines and the zero-line is omitted.

Asia, cyclonic (anticyclonic) circulations always correspond to some positive (negative) RWSs. These RWS centers are closely related to the subtropical jet (see Fig. 2c) where there is strong vorticity gradient and the RWS can be effectively produced through the vorticity advection by divergent wind $[-\mathbf{v}_\chi \cdot \nabla(\zeta + f)]$. This is consistent with the conventional understanding of the teleconnection induced by tropical heating (e.g., Trenberth et al., 1998).

## 3.4 Bias and variance quantification

In this section, we look at the impact of the biases on the simulated spatio-temporal variability in both modal and physical spaces. As elucidated in Section 2.1.2, while the total energy (kinetic energy plus potential energy) remains conserved under weak SST biases, the available potential energy, as well as the kinetic energy, does not. In addition, the TROP and EXTR balanced biases, implied by their vertical structures, have different origins and dynamics and may have different influences on the simulated variability. Therefore, we first separate them before discussing the variability changes.

### 3.4.1 TROP-EXTR separation of the balanced biases

The separation is performed in the modal space with the aid of the $Z$ profiles (the third component of the Hough vector). Although NMFs are global functions, they do have local features. Figure 8a displays some $Z$ profiles of the Rossby modes. One can see that their structures depend on the mode index $\nu = (k, n, m)$. In general, the $Z$ maxima (or minima) shift equatorward with $m$ and $k$ and move poleward with $n$. The latitude of $Z$ maximum (or minimum) indicates the action center of the Rossby modes. In this study, we classify the Rossby mode that has its $Z$ maximum (or minimum) located between 25° S and 25° N as the TROP mode, otherwise we put it in the EXTR category. We also used latitude $\pm 30°$ as the separation criterion and got the same results.

Figure 8b shows the separation in the meridional and vertical mode index plane at zonal wavenumber $k = 1$. We see that all modes with vertical index $m = 1$ or 2 (i.e., the tropospheric barotropic modes) are identified as the EXTR modes, consistent with the observations that the extratropical Rossby waves are generally barotropic (see Fig. 6). But note that the extratropical biases are not purely barotropic. As the meridional index $n$ increases, baroclinic modes go into the EXTR regime. Also note that the structure of $Z$ depends on $k$ as well, but it changes slowly with $k$. Indeed, the separations are almost identical among zonal wavenumbers $k < 7$ (not shown). Finally, 1337 TROP modes and 6493 EXTR modes are identified (the zonal-mean modes and the MRG modes are excluded in the classification). The TROP and EXTR balanced biases are then reconstructed with the Hough coefficients of the corresponding categories.

An example of the reconstructed TROP and EXTR biases from EXP_POS is shown in Figs. 8c-8f. As expected, the TROP biases are confined in the tropics which are characterized by baroclinic equatorial Rossby waves (Figs. 8c and 8d). The EXTR biases are dominated by mid-to-high latitude barotropic systems, with tropical signals being very weak (Figs. 8e and 8f). Nevertheless, there is no clear geographical boundary between the TROP and EXTR biases. The TROP-EXTR separation can benefit us in understanding both local and remote impacts of these biases on the spatio-temporal variability.
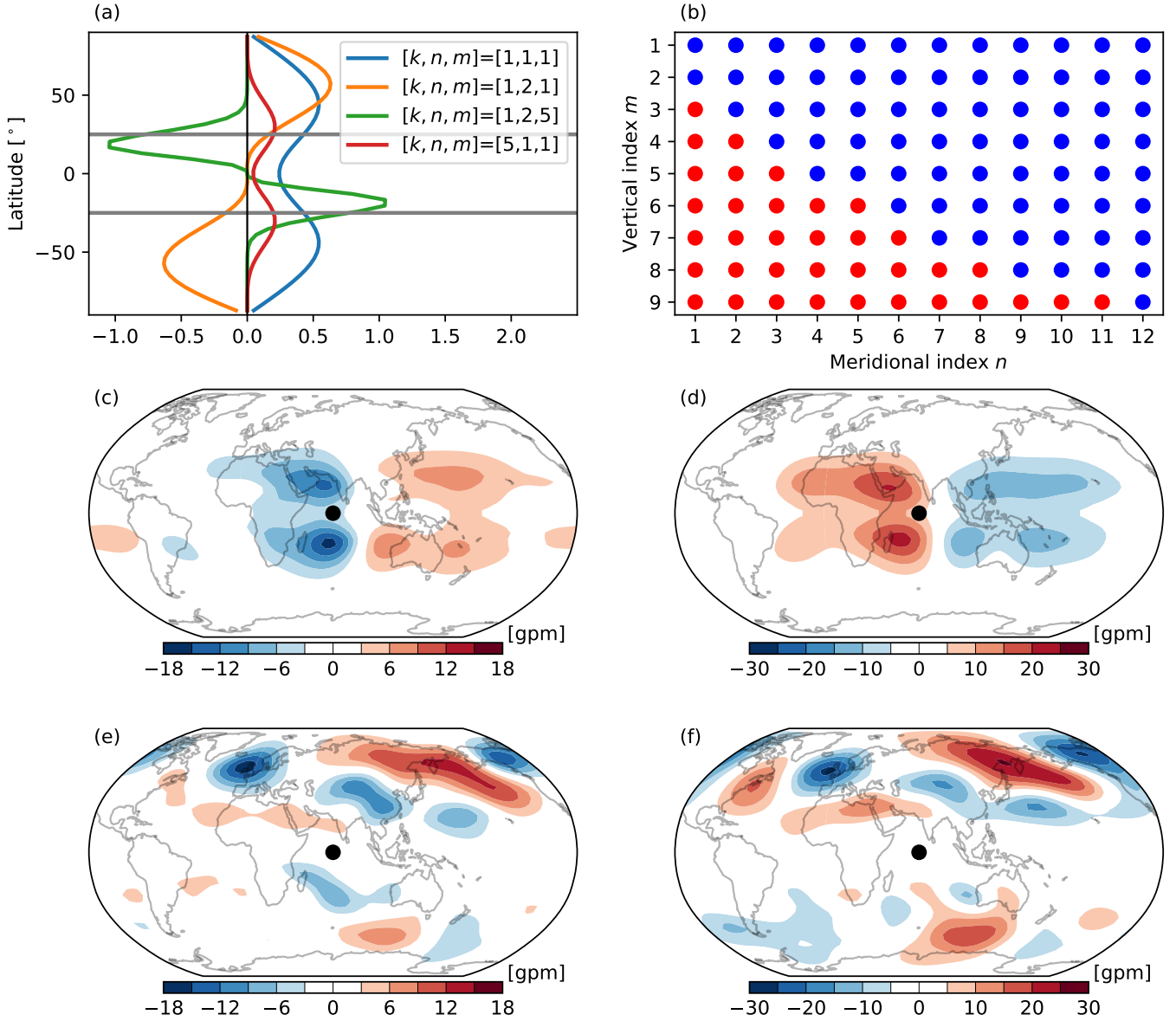
**Figure 8.** (a) Examples of the $Z$ profile of the Rossby mode. Gray lines mark the latitudes $\pm25°$. (b) Classification of the TROP and EXTR modes in modal space at zonal wavenumber $k = 1$ based on $Z$ profiles. Red (blue) dots denote the TROP (EXTR) modes. (c-d) Reconstructions of the TROP balanced geopotential height biases (m) in EXP_POS at (c) $\sigma = 0.924$ and (d) $\sigma = 0.211$. (e-f) Same as (c-d), but for the EXTR biases.
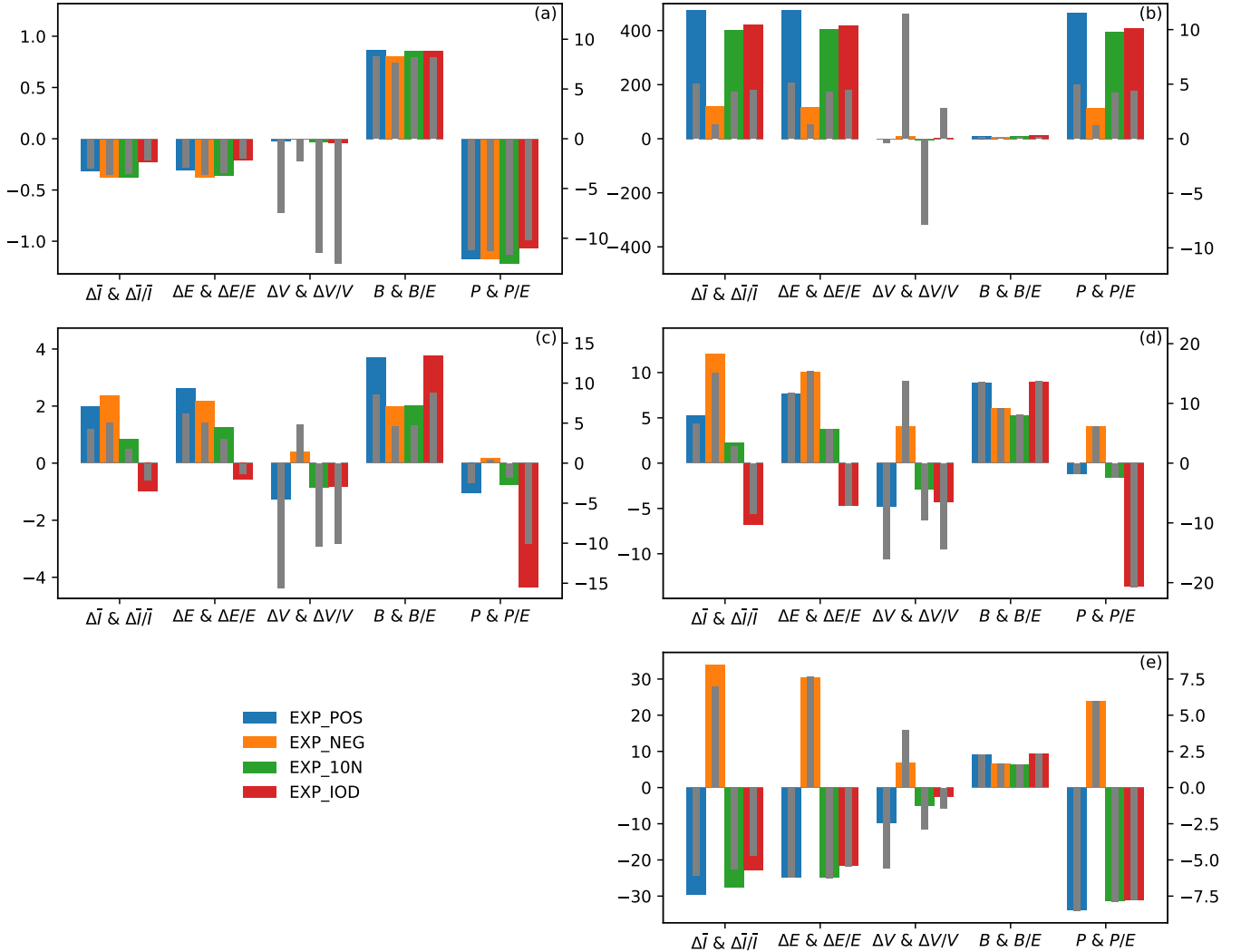
**Figure 9.** Absolute (wide bars) and relative (narrow bars) changes of the energy ($\overline{I}$ and $E$) and the interannual variance ($V$). $B$ and $P$ are the two components of $\Delta E$ (see Eq. (16)). The left panels show the results of the unbalanced (a) zonal-mean ($k = 0$) modes and (c) wave ($k > 0$) modes. The right panels show the results of (b) the balanced zonal-mean ($k = 0$) modes, (d) the TROP balanced wave ($k > 0$) modes and (e) the EXTR balanced wave ($k > 0$) modes. The relative change is calculated as the absolute change divided by the respective reference state. The left ordinate indicates the absolute changes (in m$^2$ s$^{-2}$), whereas the right axis indicates the relative changes (in %).

### 3.4.2 Variance budget in modal space

Let us first discuss the overall budget (Eq. (14)). Figure 9 shows the changes of the time-mean energy ($\Delta \overline{I}$), the climatological energy ($\Delta E$) and the temporal variance ($\Delta V$). Since the DJF-mean fields are used in the computation, the temporal variance $V$ indicates the interannual variability. These quantities are calculated separately for the zonal-mean ($k = 0$) and the wave ($k > 0$) modes. The TROP and EXTR balanced wave modes are also treated separately. Positive (negative) value means increase (decrease) of the energy or variance with respect to the reference simulation.

One can find that $\overline{I}$ and $E$ have similar changes regardless of regimes, implying $E$ dominates $V$ in the $\overline{I}$ budget (Eq. (14)). For the zonal-mean ($k = 0$) modes, they decrease in the unbalanced part (Fig. 9a) whereas increase in the balanced part (Fig. 9b) in all experiments. The overall changes vary with experiments but their magnitudes are generally smaller than 5% of the reference. The decrease in the unbalanced zonal-mean energy should be attributed to the weakening of the Hadley circulation, whereas the increase in the balanced zonal-mean energy is due to the diabatic heating induced by positive SST bias and the strengthening of the westerlies in midlatitudes and the easterlies in the tropics (see Supplement).

For the wave ($k > 0$) modes, the unbalanced $\overline{I}$ and $E$ increase in all experiments except EXP_IOD (Fig. 9c), similar to that of the TROP balanced modes (Fig. 9d). It is not surprising to see the similarity between the changes of these two wave species. Because the Kelvin modes dominating the unbalanced flow and the equatorial Rossby modes dominating the TROP balanced flow form the overall response to a tropical heating (Matsuno, 1966; Gill, 1980), they change in phase. Regarding the EXTR balanced modes, $\overline{I}$ and $E$ decrease in all experiments except for the rise in EXP_NEG (Fig. 9e). This implies a different scenario of the nonlinear wave-zonal-mean flow interaction in EXP_NEG from the others. The wave circulation biases caused by SST biases can modify the zonal-mean flow, which in turn alters the nonlinear interaction between them. It is found that the biases in EXP_NEG act to strengthen the baroclinic energy transfer from zonal-mean flow to wave flow, leading to wave energy increase (not shown). The magnitudes of the relative changes in the unbalanced wave energy are generally smaller than 5% (Fig. 9c), and those in the TROP balanced wave energy range from 3% (EXP_10N) to 15% (EXP_NEG) (Fig. 9d). The relative changes of the EXTR balanced wave energy stay around 5% in all experiments (Fig. 9e).

The energy changes can be further understood through $B$ and $P$ terms, the two components of $\Delta E$ (Eq. (16)). One can see that the $P$ term dominates the $B$ term in the zonal-mean modes (Figs. 9a and 9b) as well as the EXTR balanced wave modes (Fig. 9e). In fact, the unbalanced (balanced) zonal-mean biases are out of (in) phase with the reference state (see Supplement), resulting in large negative (positive) covariance between them. This indicates the importance of the bias phase to energy changes in the zonal-mean and the EXTR balanced wave modes. Contrarily, the $B$ term dominates the $P$ term in the unbalanced wave modes (Fig. 9c) and the TROP balanced wave modes (Fig. 9d) except EXP_IOD where the opposite situation happens.

Regarding $V$, it decreases in the unbalanced zonal-mean ($k = 0$) modes in all experiments (Fig. 9a). For the balanced zonal-mean ($k = 0$) modes, $V$ increases in EXP_NEG and EXP_IOD and decreases in the other two experiments (Fig. 9b). For wave modes of all kinds, $V$ decreases in all experiments except EXP_NEG where it increases (Figs. 9c-9e), implying that positive (negative) TIO SST bias weakens (strengthens) the global interannual variability of the wave flow. Although $\Delta V$ in the zonal-

mean flow is very small compared with $\Delta \bar{I}$ and $\Delta E$, the relative change $\Delta V/V$ could be over 10% (Figs. 9a and 9b). A similar situation happens in the TROP wave modes (Figs. 9c and 9d). Comparisons between the tropical and extratropical budgets indicate that the TIO SST bias has relatively stronger influence on $V$ in the tropics (Figs. 9c and 9d) than in the extratropics (Fig. 9e) in terms of their relative changes.
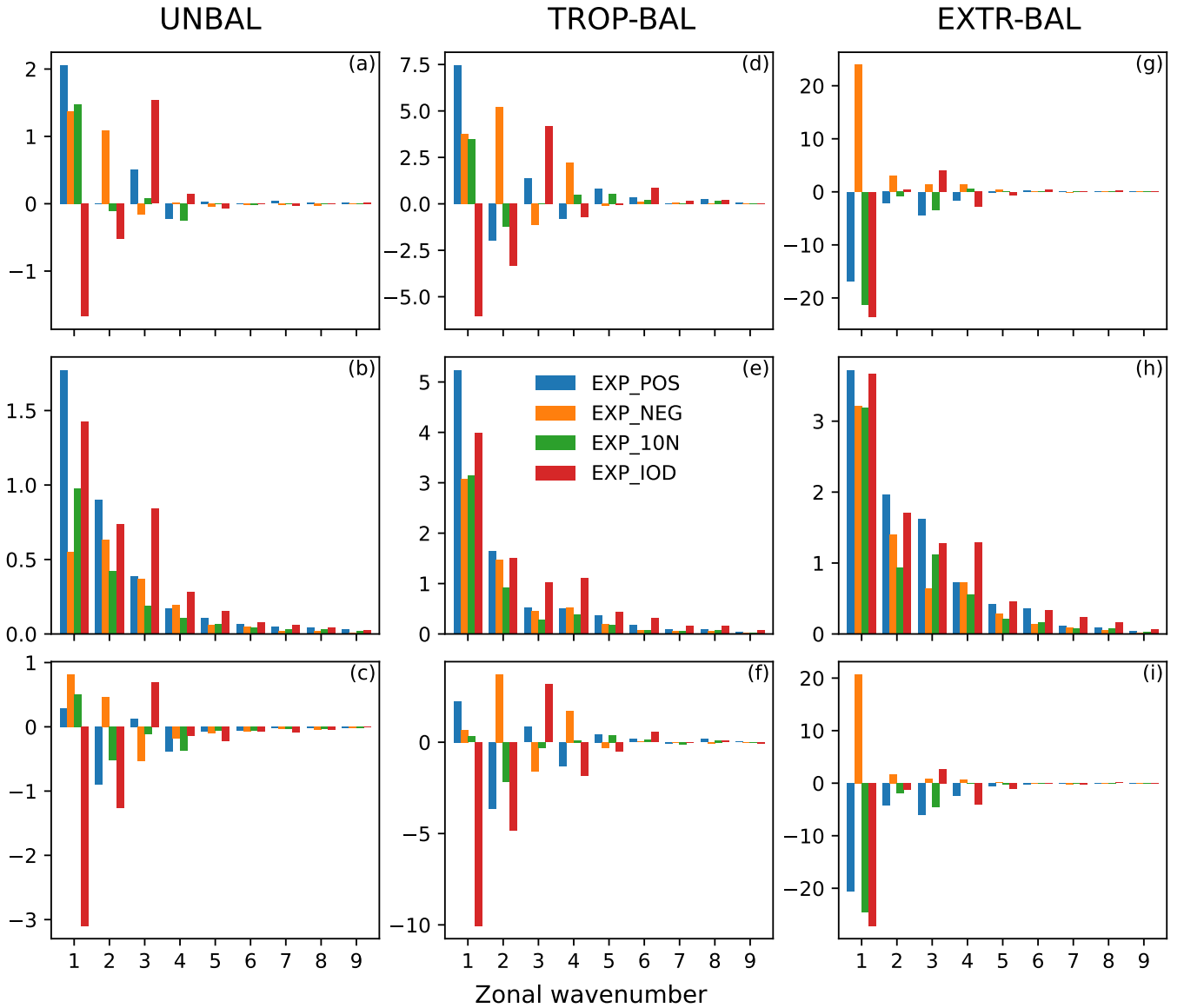
**Figure 10.** (left column) The spectra (in m$^2$ s$^{-2}$) of (a) $\Delta E$, (b) $B$ and (c) $P$ as a function of zonal wavenumber $k$ for the unbalanced modes, which have been summed over the meridional index $n$ and the vertical index $m$. (middle column) The same as left panels, but for the TROP balanced modes. (right column) The same as left panels, but for the EXTR balanced modes.

The climatological energy change $\Delta E$ with respect to the zonal wavenumber $k$ is displayed in Fig. 10, which is similar to $\Delta \overline{I}$ (not shown). For the unbalanced regime, $\Delta E$ is dominated by zonal wavenumber $k = 1$ in EXP_POS and EXP_10N (Fig. 10a), largely due to the $B$ term (Fig. 10b). In EXP_NEG, $\Delta E$ is dominated by $k = 1$ and 2, which have comparable $B$ and $P$ terms (Figs. 10b and 10c). $\Delta E$ in EXP_IOD is dominated by $k = 1 - 3$ and is mostly attributed to the $P$ term which has relatively

420 large negative values at $k = 1$ and 2 (Fig. 10c). This could be related to the large phase differences (greater than $\pi/2$) between the climatological Walker circulation and the biases caused by dipolar SST bias (see Supplement). Regarding the balanced regime, the TROP component has similar $k$-spectra to the unbalanced regime in terms of $\Delta E$, $B$, and $P$ (Figs. 10d-10f), which has been explained in preceding parts. As for the EXTR component, $\Delta E$ is dominated by $k = 1$ in all experiments (Fig. 10g), predominately due to the $P$ term (Fig. 10i).

**Table 2.** Bias variance and the percentages of selected modes. The percentage is calculated as the bias variance of the selected modes divided by the respective total amount (including $k = 0$).

| Experiments | EXP_POS | | EXP_NEG | | EXP_10N | | EXP_IOD | |
|---|---|---|---|---|---|---|---|---|
| Regimes | UNBAL | BAL | UNBAL | BAL | UNBAL | BAL | UNBAL | BAL |
| Total variance (J kg$^{-1}$) | 4.6 | 28.2 | 2.8 | 16.6 | 2.9 | 20.8 | 4.6 | 28.9 |
| $k = 0$ (%) | 19.0 | 35.9 | 28.7 | 23.4 | 29.9 | 43.5 | 18.6 | 36.5 |
| $k = 1$-5 (%) | 73.3 | 59.5 | 65.2 | 72.3 | 61.6 | 52.7 | 74.6 | 57.1 |
| $m = 1$-2 (%) | 10.9 | 24.8 | 16.6 | 28.0 | 16.5 | 28.5 | 11.0 | 29.3 |
| $m = 3$-4 (%) | 65.5 | 49.1 | 53.2 | 44.8 | 59.3 | 40.8 | 70.9 | 47.0 |
| Symmetric modes (%) | 88.1 | 77.1 | 83.2 | 73.2 | 83.0 | 73.6 | 87.9 | 73.6 |
| Kelvin (%) | 64.7 | - | 51.7 | - | 49.7 | - | 65.7 | - |
| MRG (%) | - | 0.8 | - | 0.91 | - | 0.7 | - | 1.0 |

425 Another point worth noting is the spectra of the $B$ term which indicates the bias amplitude (Figs. 10b, 10e, 10h). They seem to decay exponentially with $k$. Quantitative calculations show that 90-95% of the bias variance is stored in the first 6 zonal modes ($k = 0 - 5$; see Table 2), consistent with Žagar et al. (2020) that the representation of the SST is crucial for large scales. Besides, a large part (ranging from 73% to 88%) of the bias variance comes from the meridional symmetric modes which in the unbalanced regime are dominated by the Kelvin modes, and the MRG modes contribute less than 1% to the balanced bias

430 variance. This is even true in EXP_10N where the erroneous SST forcing is situated north of the equator. Furthermore, more bias variance comes from the baroclinic modes ($m = 3$ and 4) than the barotropic modes ($m = 1$ and 2). On the other hand, different SST biases result in different amounts of bias variance. For instance, EXP_POS and EXP_IOD have similar amount of bias variance, stronger than the other two experiments.

The interannual variance change $\Delta V$ with respect to zonal wavenumber $k$ is displayed in Fig. 11. In contrast to $\Delta E$, more

435 zonal modes engage in $\Delta V$. The unbalanced (Fig. 11a) and the TROP balanced (Fig. 11b) regimes have similar spectrum structures, albeit with different magnitudes. The zonal wavenumbers $k = 1$ and 2 dominate in EXP_POS and EXP_10N, and $k = 1 - 4$ dominate in EXP_NEG. A difference is seen in EXP_IOD, where $\Delta V$ is dominated by $k = 2$ and 3 in the unbalanced regime whereas by $k = 1$ and 2 in the TROP balanced regime. The $\Delta V$ spectra in the EXTR balanced regime differ (Fig. 11c).
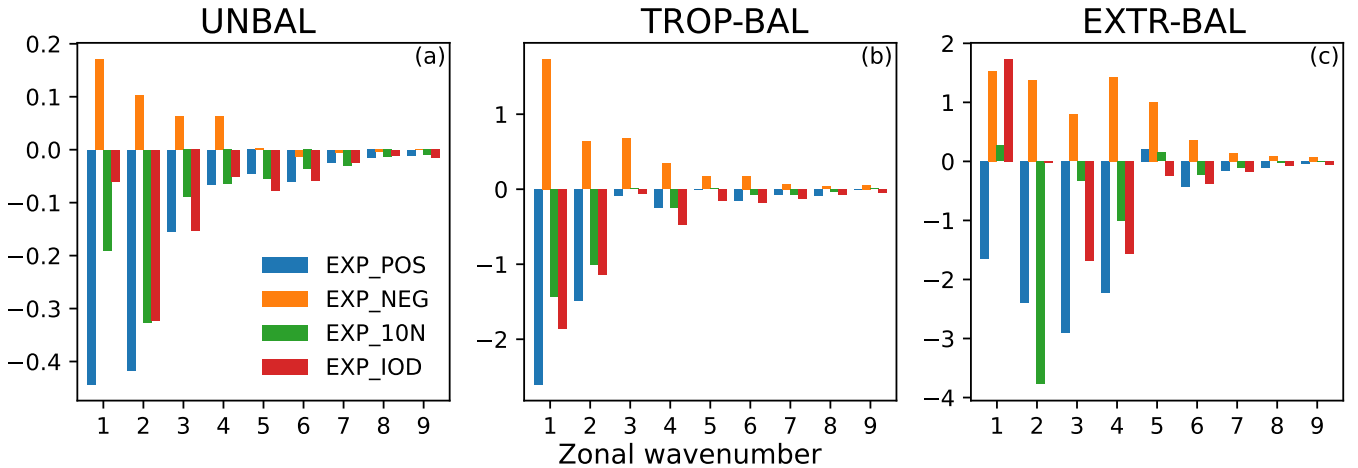
**Figure 11.** (left) The spectra (in $m^2\ s^{-2}$) of $\Delta V$ as a function of zonal wavenumber $k$ for (a) the unbalanced modes, (b) the TROP balanced modes and (c) the EXTR balanced modes. The results have been summed over the meridional index $n$ and the vertical index $m$..

One can see that $\Delta V$ is dominated by $k = 1 - 4$ in EXP_POS, by $k = 1 - 5$ in EXP_NEG, and by $k = 2$ and 4 in EXP_10N. In
EXP_IOD, $k = 1$, 3 and 4 dominate $\Delta V$, but with different signs; $k = 1$ is positive whereas the other two are negative, which
define the total change.

### 3.4.3 Interannual variance changes in physical space

The horizontal distribution of the interannual variance (IAV) changes is displayed in Fig. 12. The IAV is computed based on the
fields after the vertical projection (Eq. (12)). EXP_10N has similar distributions to EXP_POS and is thus not shown. In general,
strong IAV changes are seen in regions where the background IAVs are strong, and the distributions of the IAV changes do not
have big differences among experiments.

In the unbalanced regime, zonal winds (Fig.12a-12c) and geopotential height (not shown) dominate the IAV changes, which
have similar structures and magnitudes. We see that large IAV changes are confined in low latitudes, especially the Indo-west
Pacific region, the equatorial Atlantic and Africa, South Asia and Australia, where they can be over 25% of the reference.

In the balanced regime, large IAV changes are seen globally (Figs. 12d-12l). In low latitudes, both zonal wind and geopo-
tential height undergo large IAV changes, but their distributions are different. The IAV changes in the zonal wind are mainly
distributed along the equator in the Indo-west Pacific region (Figs. 12d-12f), whereas those in the geopotential height are seen
in subtropics, such as Middle East, South Asia, Australia and subtropical central Pacific (Figs. 12j-12l). In contrast, the absolute
IAV changes in the meridional wind are weak in the tropics, but the relative changes can be very large (over 50%), especially
in the TIO region and the Maritime Continent (Figs. 12g-12i). In mid-to-high latitudes, strong IAV changes generally occur in
the PNA sector, North Atlantic and Europe, although the locations of the change centers vary with variables. The IAV changes
of the zonal wind are mostly seen in midlatitudes, especially over the North Pacific and western Europe (Figs. 12d-12f). Those
of the meridional wind (Figs. 12g-12i) and geopotental height (Figs. 12j-12l) are confined in high latitudes, especially over
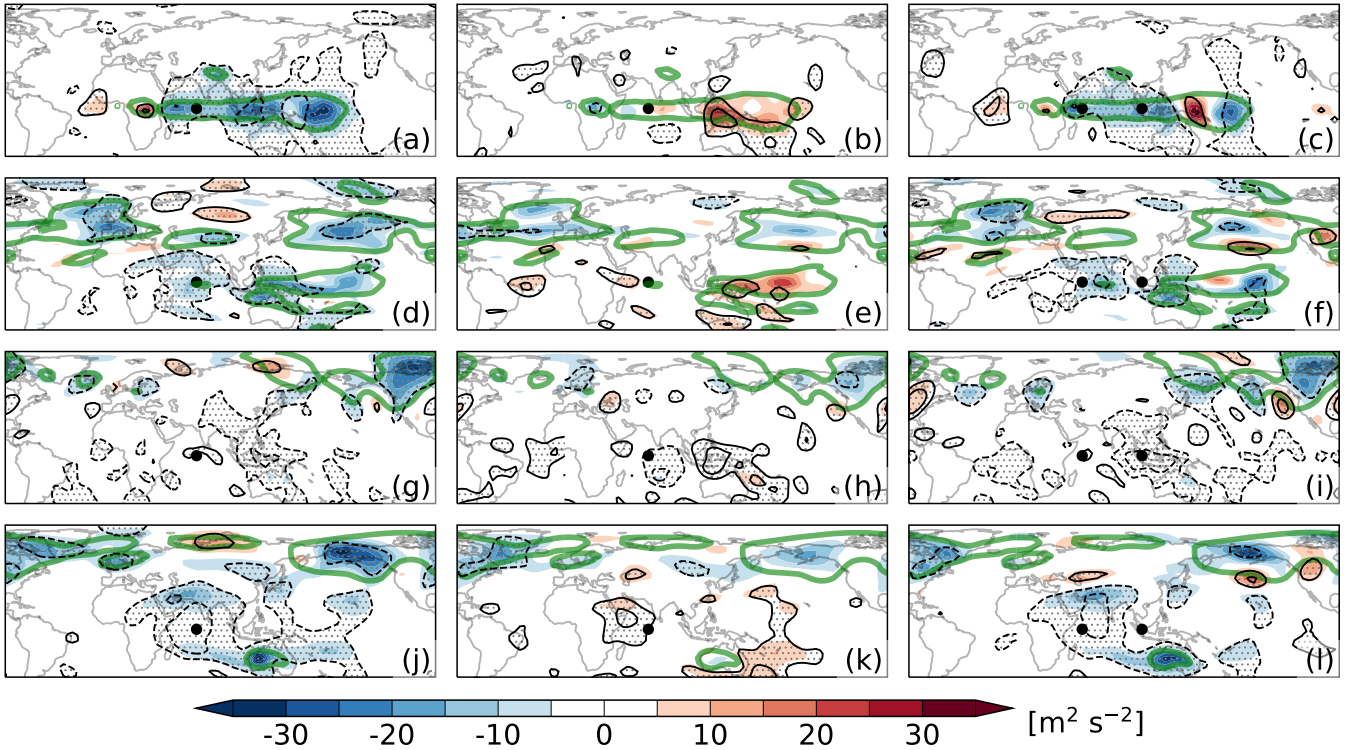
**Figure 12.** Absolute changes (colors; in m$^2$ s$^{-2}$) and relative changes (black contours; in %) of the interannual variance (summed over the vertical index $m$, i.e., $\sum_m S_m$) with respect to the reference simulation: (top row) unbalanced zonal wind, (second row) balanced zonal wind, (third row) balanced meridional wind and (bottom row) balanced geopotential height. Left column shows the results from EXP_POS, middle column from EXP_NEG, and right column from EXP_IOD. The zonal-mean modes are excluded in the computation. The absolute changes in panels (a)-(c) have been multiplied by 10 to facilitate drawing. Black contours are drawn at $\pm 25\%$ and $\pm 50\%$; negative values are indicated with dashed lines. Thick green contours show the respective reference variance at (a-c) 3, (d-f) 30, (g-i) 30 and (j-l) 40 m$^2$ s$^{-2}$, respectively.

Alaska, North America, North Europe and Northeast Asia. The IAV changes in the extratropics should be attributed to the
460  impact of the EXTR balanced biases on wave and zonal-mean flow interaction (see Fig. 7). The EXTR balanced biases (i.e., stationary Rossby waves) could modify the background flow (e.g., jet stream), which in turn affects the nonlinear interaction between them, leading to changes in both energy and interannual variability (e.g., Lau and Nath, 1991; Wettstein and Wallace, 2010; Zhao and Liang, 2018).

## 4   Conclusions and outlook

465  This study investigated both the local and remote effects of regional SST biases in the tropical Indian Ocean (TIO) based on century long (1901-2010) simulations by PLASIM, a GCM of intermediate complexity. Motivated by results from CMIP5

and CMIP6 simulations, the SST biases were prescribed as monopole or dipole anomalies with maximal amplitudes of $\pm 1.5$ K in the TIO region, superimposed on the monthly SST from ERA-20C reanalyses. The effects of the TIO SST biases enter the atmosphere through moisture and heat fluxes at the surface, thereby affecting local precipitation and generating local and remote changes in the circulation. These effects are termed "bias teleconnections". For simplicity, we investigated the bias teleconnections with a focus on boreal wintertime (December-January-February; DJF). While simplified with respect to the real atmosphere and coupled climate models, the application of PLASIM with prescribed SST provides a framework for understanding the changes in spatio-temporal variability associated with systematical errors in regional SST.

The results show that the bias teleconnections caused by the TIO SST biases are similar to the steady state response to tropical diabatic heating. In general, the TIO SST biases induce circulation biases that have the structure resembling the Gill-Matsuno pattern in the tropics and Rossby wave-train distribution in the extratropics, especially over the Pacific-North American (PNA) sector. The teleconnection between the tropical and extratropical biases is set up by Rossby wave activity flux emanating from the subtropical areas with strong Rossby wave sources. The biases mainly reside at large scales, with over 90% of the bias variance (or squared amplitude) in zonal wavenumbers $k < 6$. Comparisons among experiments show that the northward shift of the SST bias away from the equator weakens the atmospheric response, but does not change its overall structure. Besides, the positive SST bias produces stronger bias teleconnections than the negative one of the same size and magnitude.

Our methodology also provides scale- and regime-decomposed biases in the atmospheric energy and interannual variance (IAV). The energy bias of the time-mean state can be represented as the sum of the bias variance and bias covariance, which measure the amplitude and phase, respectively, of the circulation bias. In addition, the energy bias is shown to be the difference between the bias in the time-mean energy (or spatial variance) and half the bias in the IAV (or transient energy).

The changes in atmospheric energy (i.e., spatial variance) induced by the TIO SST biases are analyzed separately for the zonal-mean ($k = 0$) part and the wave ($k > 0$) part of the balanced and unbalanced components of the circulation. Across all experiments, the balanced zonal-mean flow energy increases by up to 5% compared to the reference state, whereas the unbalanced part (only 0.1% of its balanced counterpart) decreases by up to 3%. These changes primarily arise from the covariance between the circulation bias and the reference state, which results in a weakening of the Hadley circulation in the unbalanced regime and a strengthening of the zonal-mean westerlies (easterlies) in the midlatitudes (tropics) in the balanced regime.

The wave energy response to the TIO SST bias is decomposed into three components: the unbalanced part, which is confined in the tropics, and the tropical (25°S-25°N) and extratropical balanced parts. The tropical wave energies in unbalanced and balanced regimes exhibit an in-phase response. They increase in experiments with a monopolar SST bias and decrease in the case with a dipolar SST bias. The increase is mainly due to bias variance, while the decrease is due to a strong negative covariance between the bias in unbalanced circulation and the reference state (characterized by Walker circulation) at zonal wavenumbers 1 and 2. In contrast, changes in the extratropical balanced wave energy depend on the sign of the SST bias. The positive SST bias (including the dipolar case) leads to an energy decrease, while the negative SST bias results in an energy increase. The primary factor contributing to the changes (decrease or increase) is the bias covariance at zonal wavenumber 1.

The IAV responses are contingent upon the sign of the SST bias. We found that the positive SST bias can lead to reductions in the IAV of up to 15% for the unbalanced wave flow, 16% for the tropical balanced wave flow, and 6% for the extratropical

balanced wave flow, respectively, compared to their respective reference states. The negative SST bias has the opposite effect, causing an increase in the IAV by up to 5% for the unbalanced wave flow, 14% for the tropical balanced wave flow, and 4% for the extratropical balanced wave flow, respectively. In contrast to the energy response, changes in the IAV due to the TIO SST biases are spread across more zonal scales, with visible changes not only at planetary scales but also at zonal wavenumbers 4 and 5. Geographically, the IAV responses to the TIO SST bias are predominantly confined to the Indo-west Pacific region, Australia, South and Northeast Asia, the Pacific-North America region and Europe, where the background IAVs are strong.

In summary, we conducted a thorough investigation of the bias teleconnections induced by SST biases in the TIO region and their impacts on model circulation and variability. Our paper provides a novel dynamical framework for evaluating simulations of CGCMs, such as CMIP models, that have suffered from severe SST biases over time. In the case of TIO SST biases, only positive SST biases are detrimental for the global zonal-mean circulation. In contrast, the responses of the wave circulation and its IAV depend on the sign of the SST bias. The IAVs of wave flows are reduced (enhanced) by the positive (negative) SST bias. In addition, the responses of the tropical wave energies are related to the spatial structure of the SST bias, with the monopolar (dipolar) SST bias increasing (decreasing) the tropical wave energies.

Finally, the simplifications of this study need to be mentioned. Using an atmosphere-only GCM forced with prescribed SST eliminates any feedback from the atmosphere to the ocean. While this simplifies the problem under study, it reduces the reality of simulated processes in the TIO region. In fact, the SST variability in the region is coherent with monsoon variability with a phase relation consistent with a coupled oscillation (Vecchi and Harrison, 2002), which is absent from the atmosphere-only GCM. The coupling between the SST and the precipitation (deep convection) could therefore be more complicated than depicted in this study. Furthermore, the TIO has warmed faster than any other tropical oceans over the past century (Roxy et al., 2020), and the atmospheric bias teleconnections associated with the TIO SST bias may have a temporal evolution with the non-stationary background SST. While not addressed in this paper, it will be discussed in follow-on studies. On the other hand, SST biases in different regions are likely to result in different bias teleconnections (e.g., Barsugli and Sardeshmukh, 2002; Zhou et al., 2017; Thomson and Vallis, 2018). Our future work will extend the approach developed in this study to other regions of the global oceans to quantify the sensitivity of the atmospheric bias teleconnections to the location of the SST bias.

*Code and data availability.* All data used in this work can be obtained from Y.-B. Zhao through email. The PLASIM source code and detailed userguide can be downloaded at https://www.mi.uni-hamburg.de/en/arbeitsgruppen/theoretische-meteorologie/modelle/plasim.html. The MODES package can be requested via https://modes.cen.uni-hamburg.de.

*Author contributions.* YBZ and NŽ designed the study and YBZ carried them out. All co-authors contributed to interpreting the results. YBZ prepared the manuscript with contributions from all co-authors.

*Competing interests.* The authors declare that they have no conflict of interest.

*Acknowledgements.* This work is a contribution to project S1 of the Collaborative Research Centre TRR 181 "Energy Transfer in Atmosphere and Ocean" funded by the Deutsche Forschungsgemeinschaft (DFG, German Research Foundation) under project number 274762653.

530

# References

535    Annamalai, H., Okajima, H., and Watanabe, M.: Possible Impact of the Indian Ocean SST on the Northern Hemisphere Circulation during El Niño, Journal of Climate, 20, 3164–3189, https://doi.org/10.1175/JCLI4156.1, 2007.

Annamalai, H., Taguchi, B., McCreary, J. P., Nagura, M., and Miyama, T.: Systematic Errors in South Asian Monsoon Simulation: Importance of Equatorial Indian Ocean Processes, Journal of Climate, 30, 8159–8178, https://doi.org/10.1175/JCLI-D-16-0573.1, 2017.

Back, L. E. and Bretherton, C. S.: On the Relationship between SST Gradients, Boundary Layer Winds, and Convergence over the Tropical
540    Oceans, Journal of Climate, 22, 4182–4196, https://doi.org/10.1175/2009JCLI2392.1, 2009.

Bai, H., Li, B., Mehra, A., Meixner, J., Moorthi, S., Ray, S., Stefanova, L., Wang, J., Wang, J., Worthen, D., Yang, F., and Stan, C.: The impact of tropical SST biases on the S2S precipitation forecast skill over the Contiguous United States in the UFS global coupled model, Weather and Forecasting, in press, https://doi.org/https://doi.org/10.1175/WAF-D-22-0162.1, 2023.

Barsugli, J. J. and Sardeshmukh, P. D.: Global atmospheric sensitivity to tropical SST anomalies throughout the Indo-Pacific basin, Journal
545    of Climate, 15, 3427–3442, https://doi.org/10.1175/1520-0442(2002)015<3427:GASTTS>2.0.CO;2, 2002.

Beal, L. M., Vialard, J., Roxy, M. K., Li, J., Andres, M., Annamalai, H., Feng, M., Han, W., Hood, R., Lee, T., Lengaigne, M., Lumpkin, R., Masumoto, Y., McPhaden, M. J., Ravichandran, M., Shinoda, T., Sloyan, B. M., Strutton, P. G., Subramanian, A. C., Tozuka, T., Ummenhofer, C. C., Unnikrishnan, A. S., Wiggert, J., Yu, L., Cheng, L., Desbruyères, D. G., and Parvathi, V.: A Road Map to IndOOS-2: Better Observations of the Rapidly Warming Indian Ocean, Bulletin of the American Meteorological Society, 101, E1891–E1913,
550    https://doi.org/10.1175/BAMS-D-19-0209.1, 2020.

Bollasina, M. A. and Ming, Y.: The general circulation model precipitation bias over the southwestern equatorial Indian Ocean and its implications for simulating the South Asian monsoon, Climate Dynamics, 40, 823–838, https://doi.org/10.1007/s00382-012-1347-7, 2013.

Cai, W. and Cowan, T.: Why is the amplitude of the Indian Ocean Dipole overly large in CMIP3 and CMIP5 climate models?, Geophysical Research Letters, 40, 1200–1205, https://doi.org/10.1002/grl.50208, 2013.

555    Castanheira, J. M. and Marques, C. A. F.: Biases of the Barotropic Atmospheric Circulation Variability in CMIP6 Models, Journal of Climate, 35, 5071–5085, https://doi.org/10.1175/JCLI-D-21-0581.1, 2022.

Eliassen, E., Machenhauer, B., and Rasmusson, E.: On a numerical method for integration of the hydrodynamical equations with a spectral representation of the horizontal fields, 1970.

Fathrio, I., Iizuka, S., Manda, A., Kodama, Y.-M., Ishida, S., Moteki, Q., Yamada, H., and Tachibana, Y.: Assessment of western Indian
560    Ocean SST bias of CMIP5 models, Journal of Geophysical Research: Oceans, 122, 3123–3140, https://doi.org/10.1002/2016JC012443, 2017.

Fraedrich, K. and Lunkeit, F.: Diagnosing the entropy budget of a climate model, Tellus A: Dynamic Meteorology and Oceanography, 60, 921–931, https://doi.org/10.1111/j.1600-0870.2008.00338.x, 2008.

Fraedrich, K., Jansen, H., Kirk, E., Luksch, U., and Lunkeit, F.: The Planet Simulator: Towards a user friendly model, Meteorologische
565    Zeitschrift, pp. 299–304, https://doi.org/10.1127/0941-2948/2005/0043, 2005.

Gadgil, S., Joseph, P. V., and Joshi, N. V.: Ocean–atmosphere coupling over monsoon regions, Nature, 312, 141–143, https://doi.org/10.1038/312141a0, 1984.

Gill, A. E.: Some simple solutions for heat-induced tropical circulation, Quarterly Journal of the Royal Meteorological Society, 106, 447–462, https://doi.org/10.1002/qj.49710644905, 1980.

Hermes, J. C., Masumoto, Y., Beal, L. M., Roxy, M. K., Vialard, J., Andres, M., Annamalai, H., Behera, S., D'Adamo, N., Doi, T., Feng, M., Han, W., Hardman-Mountford, N., Hendon, H., Hood, R., Kido, S., Lee, C., Lee, T., Lengaigne, M., Li, J., Lumpkin, R., Navaneeth, K. N., Milligan, B., McPhaden, M. J., Ravichandran, M., Shinoda, T., Singh, A., Sloyan, B., Strutton, P. G., Subramanian, A. C., Thurston, S., Tozuka, T., Ummenhofer, C. C., Unnikrishnan, A. S., Venkatesan, R., Wang, D., Wiggert, J., Yu, L., and Yu, W.: A Sustained Ocean Observing System in the Indian Ocean for Climate Related Scientific Knowledge and Societal Needs, Frontiers in Marine Science, 6, 2019.

Joseph, S., Sahai, A. K., Goswami, B. N., Terray, P., Masson, S., and Luo, J.-J.: Possible role of warm SST bias in the simulation of boreal summer monsoon in SINTEX-F2 coupled model, Climate Dynamics, 38, 1561–1576, https://doi.org/10.1007/s00382-011-1264-1, 2012.

Kosovelj, K., Kucharski, F., Molteni, F., and Žagar, N.: Modal Decomposition of the Global Response to Tropical Heating Perturbations Resembling MJO, Journal of the Atmospheric Sciences, 76, 1457 – 1469, https://doi.org/10.1175/JAS-D-18-0203.1, 2019.

Kuo, H. L.: On Formation and Intensification of Tropical Cyclones Through Latent Heat Release by Cumulus Convection., Journal of Atmospheric Sciences, 22, 40–63, https://doi.org/10.1175/1520-0469(1965)022<0040:OFAIOT>2.0.CO;2, 1965.

Kuo, H. L.: Further Studies of the Parameterization of the Influence of Cumulus Convection on Large-Scale Flow., Journal of Atmospheric Sciences, 31, 1232–1240, https://doi.org/10.1175/1520-0469(1974)031<1232:FSOTPO>2.0.CO;2, 1974.

Lacis, A. A. and Hansen, J.: A Parameterization for the Absorption of Solar Radiation in the Earth's Atmosphere., Journal of Atmospheric Sciences, 31, 118–133, https://doi.org/10.1175/1520-0469(1974)031<0118:APFTAO>2.0.CO;2, 1974.

Lau, N.-C. and Nath, M. J.: Variability of the Baroclinic and Barotropic Transient Eddy Forcing Associated with Monthly Changes in the Midlatitude Storm Tracks, Journal of Atmospheric Sciences, 48, 2589 – 2613, https://doi.org/10.1175/1520-0469(1991)048<2589:VOTBAB>2.0.CO;2, 1991.

Laursen, L. and Eliasen, E.: On the effects of the damping mechanisms in an atmospheric general circulation model, Tellus Series A, 41, 385–400, https://doi.org/10.3402/tellusa.v41i5.11848, 1989.

Levine, R. C. and Turner, A. G.: Dependence of Indian monsoon rainfall on moisture fluxes across the Arabian Sea and the impact of coupled model sea surface temperature biases, Climate Dynamics, 38, 2167–2190, https://doi.org/10.1007/s00382-011-1096-z, 2012.

Li, G. and Xie, S.-P.: Origins of tropical-wide SST biases in CMIP multi-model ensembles, Geophysical Research Letters, 39, https://doi.org/10.1029/2012GL053777, 2012.

Li, G., Xie, S.-P., and Du, Y.: Monsoon-Induced Biases of Climate Models over the Tropical Indian Ocean, Journal of Climate, 28, 3058–3072, https://doi.org/10.1175/JCLI-D-14-00740.1, 2015.

Lindzen, R. S. and Nigam, S.: On the Role of Sea Surface Temperature Gradients in Forcing Low-Level Winds and Convergence in the Tropics, Journal of the Atmospheric Sciences, 44, 2418–2436, https://doi.org/10.1175/1520-0469(1987)044<2418:OTROSS>2.0.CO;2, 1987.

Louis, J.-F.: A parametric model of vertical eddy fluxes in the atmosphere, Boundary-Layer Meteorology, 17, 187–202, https://doi.org/10.1007/BF00117978, 1979.

Louis, J.-F., Tiedtke, M., and Geleyn, M.: A short history of the PBL parameterisationv at ECMWF, in: Proceedings, ECMWF workshop on planetary boundary layer parameterization, pp. 59–80, Amer. Meteor. Soc., Reading, 1982.

Lunkeit, F. and von Detten, Y.: The linearity of the atmospheric response to North Atlantic sea surface temperature anomalies, Journal of climate, 10, 3003–3014, https://doi.org/10.1175/1520-0442(1997)010<3003:TLOTAR>2.0.CO;2, 1997.

Lyon, B.: Biases in CMIP5 Sea Surface Temperature and the Annual Cycle of East African Rainfall, Journal of Climate, 33, 8209–8223, https://doi.org/10.1175/JCLI-D-20-0092.1, 2020.

Matsuno, T.: Quasi-Geostrophic Motions in the Equatorial Area, Journal of the Meteorological Society of Japan. Ser. II, 44, 25–43, https://doi.org/10.2151/jmsj1965.44.1_25, 1966.

610 McKenna, S., Santoso, A., Gupta, A. S., Taschetto, A. S., and Cai, W.: Indian Ocean Dipole in CMIP5 and CMIP6: characteristics, biases, and links to ENSO, Scientific Reports, 10, 11 500, https://doi.org/10.1038/s41598-020-68268-9, 2020.

Orszag, S. A.: Transform Method for the Calculation of Vector-Coupled Sums: Application to the Spectral Form of the Vorticity Equation., Journal of Atmospheric Sciences, 27, 890–895, https://doi.org/10.1175/1520-0469(1970)027<0890:TMFTCO>2.0.CO;2, 1970.

Pikovnik, M., Zaplotnik, Ž., Boljka, L., and Žagar, N.: Metrics of the Hadley circulation strength and associated circulation trends, Weather

615 and Climate Dynamics, 3, 625–644, https://doi.org/10.5194/wcd-3-625-2022, 2022.

Plumb, R. A.: On the Three-Dimensional Propagation of Stationary Waves, Journal of Atmospheric Sciences, 42, 217 – 229, https://doi.org/10.1175/1520-0469(1985)042<0217:OTTDPO>2.0.CO;2, 1985.

Poli, P., Hersbach, H., Dee, D. P., Berrisford, P., Simmons, A. J., Vitart, F., Laloyaux, P., Tan, D. G. H., Peubey, C., Thépaut, J.-N., Trémolet, Y., Hólm, E. V., Bonavita, M., Isaksen, L., and Fisher, M.: ERA-20C: An Atmospheric Reanalysis of the Twentieth Century, Journal of

620 Climate, 29, 4083 – 4097, https://doi.org/10.1175/JCLI-D-15-0556.1, 2016.

Prodhomme, C., Terray, P., Masson, S., Izumo, T., Tozuka, T., and Yamagata, T.: Impacts of Indian Ocean SST biases on the Indian Monsoon: as simulated in a global coupled model, Climate Dynamics, 42, 271–290, https://doi.org/10.1007/s00382-013-1671-6, 2014.

Roeckner, E., Arpe, K., Bengtsson, L., Brinkop, S., Dumenil, L., Esch, M., Kirk, E., Lunkeit, F., Ponater, M., Rockel, B., Sausen, R., Schlese, U., Schubert, S., and Windelband, M.: Simulation of the present-day climate with the ECHAM-3 model: Impact of model physics and

625 resolution, 1992.

Roxy, M., Gnanaseelan, C., Parekh, A., Chowdary, J. S., Singh, S., Modi, A., Kakatkar, R., Mohapatra, S., Dhara, C., Shenoi, S., et al.: Indian ocean warming, Assessment of Climate Change over the Indian Region: A Report of the Ministry of Earth Sciences (MoES), Government of India, pp. 191–206, https://doi.org/https://doi.org/10.1007/978-981-15-4327-2_10, 2020.

Roxy, M. K., Ritika, K., Terray, P., and Masson, S.: The Curious Case of Indian Ocean Warming, Journal of Climate, 27, 8501–8509,

630 https://doi.org/10.1175/JCLI-D-14-00471.1, 2014.

Sardeshmukh, P. D. and Hoskins, B. J.: The Generation of Global Rotational Flow by Steady Idealized Tropical Divergence, Journal of Atmospheric Sciences, 45, 1228 – 1251, https://doi.org/10.1175/1520-0469(1988)045<1228:TGOGRF>2.0.CO;2, 1988.

Sasamori, T.: The Radiative Cooling Calculation for Application to General Circulation Experiments., Journal of Applied Meteorology, 7, 721–729, https://doi.org/10.1175/1520-0450(1968)007<0721:TRCCFA>2.0.CO;2, 1968.

635 Schott, F. A., Xie, S.-P., and McCreary, J. P.: Indian Ocean circulation and climate variability, Reviews of Geophysics, 47, RG1002, https://doi.org/10.1029/2007RG000245, 2009.

Slingo, A. and Slingo, J. M.: Response of the National Center for Atmospheric Research community climate model to improvements in the representation of clouds, J. Geoph. Res., 96, 15,341–15,357, https://doi.org/10.1029/91JD00930, 1991.

Stan, C., Krishnamurthy, V., Bai, H., Li, B., Mehra, A., Meixner, J., Moorthi, S., Stefanova, L., Wang, J., Wang, J., Worthen, D., and Yang,

640 F.: The Impact of Tropical Pacific SST Biases on the S2S Forecast Skill over North America in the UFS Global Coupled Model, Journal of Climate, 36, 2439–2456, https://doi.org/10.1175/JCLI-D-22-0196.1, 2023.

Stephens, G. L.: Radiation Profiles in Extended Water Clouds. II: Parameterization Schemes., Journal of Atmospheric Sciences, 35, 2123–2132, https://doi.org/10.1175/1520-0469(1978)035<2123:RPIEWC>2.0.CO;2, 1978.

Stephens, G. L.: The Parameterization of Radiation for Numerical Weather Prediction and Climate Models, Monthly Weather Review, 112,

645 826, https://doi.org/10.1175/1520-0493(1984)112<0826:TPORFN>2.0.CO;2, 1984.

Thomson, S. I. and Vallis, G. K.: Atmospheric response to SST anomalies. Part I: Background-state dependence, teleconnections, and local effects in winter, Journal of the Atmospheric Sciences, 75, 4107–4124, https://doi.org/10.1175/JAS-D-17-0297.1, 2018.

Trenberth, K. E., Branstator, G. W., Karoly, D., Kumar, A., Lau, N.-C., and Ropelewski, C.: Progress during TOGA in understanding and modeling global teleconnections associated with tropical sea surface temperatures, Journal of Geophysical Research: Oceans, 103, 14 291–14 324, https://doi.org/https://doi.org/10.1029/97JC01444, 1998.

Turner, A. G., Inness, P. M., and Slingo, J. M.: The role of the basic state in the ENSO-monsoon relationship and implications for predictability, Quarterly Journal of the Royal Meteorological Society, 131, 781–804, https://doi.org/10.1256/qj.04.70, 2005.

Vecchi, G. A. and Harrison, D. E.: Monsoon Breaks and Subseasonal Sea Surface Temperature Variability in the Bay of Bengal, Journal of Climate, 15, 1485–1493, https://doi.org/10.1175/1520-0442(2002)015<1485:MBASSS>2.0.CO;2, 2002.

Žagar, N., Kasahara, A., Terasaki, K., Tribbia, J., and Tanaka, H.: Normal-mode function representation of global 3-D data sets: open-access software for the atmospheric research community, Geoscientific Model Development, 8, 1169–1195, https://doi.org/10.5194/gmd-8-1169-2015, 2015.

Žagar, N., Kosovelj, K., Manzini, E., Horvat, M., and Castanheira, J.: An assessment of scale-dependent variability and bias in global prediction models, Climate Dynamics, 54, 287–306, https://doi.org/10.1007/s00382-019-05001-x, 2020.

Wang, C., Zhang, L., Lee, S.-K., Wu, L., and Mechoso, C. R.: A global perspective on CMIP5 climate model biases, Nature Climate Change, 4, 201–205, https://doi.org/10.1038/nclimate2118, 2014.

Wang, Y., Heywood, K. J., Stevens, D. P., and Damerell, G. M.: Seasonal extrema of sea surface temperature in CMIP6 models, Ocean Science, 18, 839–855, https://doi.org/10.5194/os-18-839-2022, 2022.

Weller, E. and Cai, W.: Asymmetry in the IOD and ENSO Teleconnection in a CMIP5 Model Ensemble and Its Relevance to Regional Rainfall, Journal of Climate, 26, 5139–5149, https://doi.org/10.1175/JCLI-D-12-00789.1, 2013.

Wettstein, J. J. and Wallace, J. M.: Observed Patterns of Month-to-Month Storm-Track Variability and Their Relationship to the Background Flow, Journal of the Atmospheric Sciences, 67, 1420 – 1437, https://doi.org/10.1175/2009JAS3194.1, 2010.

Zhang, Q., Liu, B., Li, S., and Zhou, T.: Understanding Models' Global Sea Surface Temperature Bias in Mean State: From CMIP5 to CMIP6, Geophysical Research Letters, 50, e2022GL100 888, https://doi.org/https://doi.org/10.1029/2022GL100888, 2023.

Zhang, Y. and Liang, X. S.: The distinct PNA pattern induced by the South China Sea, Climate Dynamics, https://doi.org/10.1007/s00382-022-06607-4, 2022.

Zhao, Y.-B. and Liang, X. S.: On the Inverse Relationship between the Boreal Wintertime Pacific Jet Strength and Storm-Track Intensity, Journal of Climate, 31, 9545 – 9564, https://doi.org/10.1175/JCLI-D-18-0043.1, 2018.

Zhou, C., Zelinka, M. D., and Klein, S. A.: Analyzing the dependence of global cloud feedback on the spatial pattern of sea surface temperature change with a Green's function approach, Journal of Advances in Modeling Earth Systems, 9, 2174–2189, https://doi.org/10.1002/2017MS001096, 2017.